





RESEARCH ARTICLE

Cerebellar structural, astrocytic, and neuronal abnormalities in the SMN Δ 7 mouse model of spinal muscular atrophy

Nicholas C. Cottam¹  | Tiffany Bamfo¹ | Melissa A. Harrington²  |
Christine J. Charvet^{2,4,3}  | Khan Hekmatyar^{6,5} | Nikita Tulin⁷ | Jianli Sun^{1,2} 

¹Department of Biological Sciences, Delaware State University, Dover, Delaware, USA

²Delaware Center for Neuroscience Research, Delaware State University, Dover, Delaware, USA

³Department of Anatomy, Physiology and Pharmacology, Auburn University, Auburn, Alabama, USA

⁴Department of Psychology, Delaware State University, Dover, DE, United States

⁵Center for Biomedical and Brain Imaging, University of Delaware, Newark, Delaware, USA

⁶Bioimaging Research Center for Biomedical and Brain Imaging, University of Georgia, Athens, Georgia, USA

⁷Department of Neuroscience, Temple University, Philadelphia, Pennsylvania, USA

Correspondence

Jianli Sun, Department of Biological Sciences,
Delaware State University, 1200 N DuPont
Highway, Dover, DE 19901, USA.
Email: jianlisun@desu.edu

Funding information

Center of Biomedical Research Excellence (COBRE)—NIH, Grant/Award Number: P20GM103653; Delaware IDeA Network of Biomedical Research Excellence, Grant/Award Number: P20GM103446; National Institute of General Medical Sciences, Grant/Award Number: R25GM122722; National Institute of Neurological Disorders and Stroke, Grant/Award Numbers: R15NS120154, R25NS095371

Abstract

Spinal muscular atrophy (SMA) is a neuromuscular disease that affects as many as 1 in 6000 individuals at birth, making it the leading genetic cause of infant mortality. A growing number of studies indicate that SMA is a multi-system disease. The cerebellum has received little attention even though it plays an important role in motor function and widespread pathology has been reported in the cerebella of SMA patients. In this study, we assessed SMA pathology in the cerebellum using structural and diffusion magnetic resonance imaging, immunohistochemistry, and electrophysiology with the SMN Δ 7 mouse model. We found a significant disproportionate loss in cerebellar volume, decrease in afferent cerebellar tracts, selective lobule-specific degeneration of Purkinje cells, abnormal lobule foliation and astrocyte integrity, and a decrease in spontaneous firing of cerebellar output neurons in the SMA mice compared to controls. Our data suggest that defects in cerebellar structure and function due to decreased survival motor neuron (SMN) levels impair the functional cerebellar output affecting motor control, and that cerebellar pathology should be addressed to achieve comprehensive treatment and therapy for SMA patients.

KEYWORDS

cerebellum, magnetic resonance imaging, mouse model, neurodegeneration, Purkinje cells, spinal muscular atrophy

1 | INTRODUCTION

Spinal muscular atrophy (SMA), the leading genetic cause in infant mortality, is an autosomal recessive disease that affects 1 out of every 6000–10,000 individuals at

birth [1,2]. A deletion or mutation in survival motor neuron 1 (*SMN1*) gene causes lower motor neuron dysfunction and degeneration, leading to progressive muscle atrophy, weakness, and paralysis [3–5]. *SMN1* is the most common disease-determining gene for SMA, but an additional gene,

This is an open access article under the terms of the [Creative Commons Attribution-NonCommercial-NoDerivs](https://creativecommons.org/licenses/by-nc-nd/4.0/) License, which permits use and distribution in any medium, provided the original work is properly cited, the use is non-commercial and no modifications or adaptations are made.

© 2023 The Authors. *Brain Pathology* published by John Wiley & Sons Ltd on behalf of International Society of Neuropathology.

SMN2, can partially make up for the reduced protein levels when *SMN1* is mutated. The number of *SMN2* copies carried by SMA patients is inversely correlated to symptom severity, which is related to the age of onset, level of motor function, and patient survival time [2,6]. These factors are used clinically to classify patients into SMA types 0 through 4, with type 0 being most severe and type 4 being the least [7–10].

Sufficient SMN expression is critical to the development and physiological function of motor neurons. Within nuclei, SMN forms a large macromolecular complex (SMN complex) that is known to function in RNA and protein trafficking during dendritic and axonal development of motor neurons, as well as in the assembly of small nuclear ribonucleoproteins (snRNPs) [11,12]. It also has other proposed roles in regulating cytoskeletal dynamics, the endocytic pathway, and autophagy [7]. Reduction in SMN protein levels due to altered SMN transcripts causes lower levels of functional spliceosomal snRNPs in SMA patient cell lines [13] and SMN-deficient mice [14], with the greatest effect being observed in motor neurons [15]. However, the defects resultant of SMN deficiency is still mostly unknown across many cell types. Recent studies points toward SMA being a multi-system disease ([16–20]), with effects beyond lower motor neurons and their associated circuitry. Further investigation into the brain may provide crucial insight into understanding SMN function and the progression of SMA pathology. The spinal cord has received much attention [5,21–24] and the degeneration due to SMN deficiency in lower motor neurons of the spinal cord and at the neuromuscular junction is well-characterized [25,26]. However, SMA pathology in the upper motor neuron projections and within the brain itself remain unclear [17], highlighting the necessity to thoroughly define pathology throughout the nervous system. Doing so will help generate a complete characterization of SMA disease progression and guide the development of therapies to sustain patient brain development and quality of life.

Accumulating evidence suggests widespread SMA pathology across the brain. In severe SMA patients (Type 0 and Type 1), neuronal degeneration has been observed in the thalamus, cerebral cortex, pigmented nuclei, brainstem, and cerebellum [23,27–29]. In SMN-depleted mouse embryos, altered morphology and defasciculation of facial cranial nerve bundles has been observed [30]. In the hippocampus, where there is notably dense SMN expression [31], *SMN*^{-/-}; *SMN2* mice exhibit decreased SMN levels, as well as a decrease in cell density, cell proliferation, and neurogenesis [32]. In the thalamus of SMA type 0 patients, neurodegeneration [33] and atrophy [34] have been detected. Importantly, motor and extra-motor regions in the cortex of SMA-affected brains showed increased gray matter density [24] and a reduction of layer V pyramidal neurons [35], indicating pathological defects along cerebrospinal tracts. These studies suggest that SMA pathogenesis in the central nervous

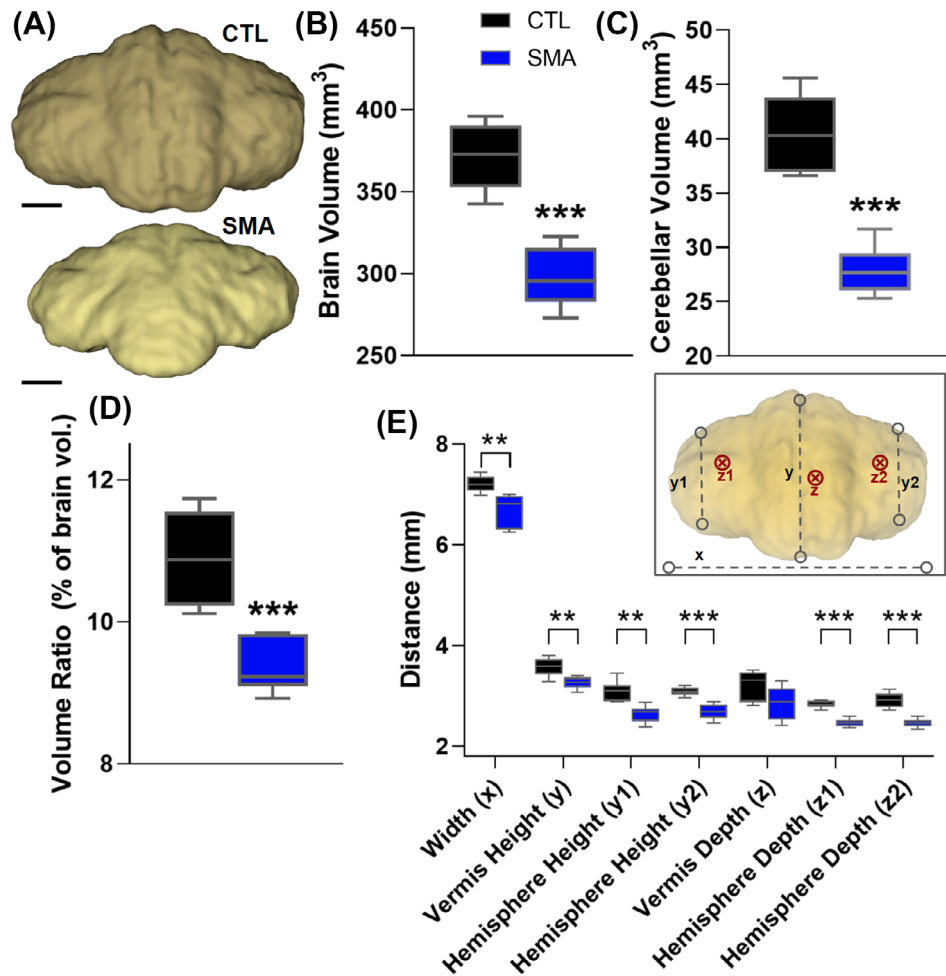
system (CNS) extends beyond spinal motor neuron degeneration. To better understand the mechanisms of SMA pathology, a more complete characterization of these brain regions impacted by SMA is required.

The cerebellum plays a key role in mediating locomotor control and is emerging as a critical region to be studied as reports of abnormalities within the cerebellum accumulate in SMA patients. The cerebellum communicates directly with integral motor circuit components such as the thalamus, motor cortex and spinal cord to precisely refine motor function. In mammalian motor circuitry, locomotion is initiated in the motor cortex and signals descend through the pyramidal and extrapyramidal tracts to the brainstem and spinal cord. Some of these tracts project to brainstem nuclei and integrate into the cerebellum via the middle peduncles. The proprioceptive signals necessary for motor refinement originate from the muscle spindles and tendon organs, ascend to the spinal cord, and project to the cerebellum through inferior peduncles. These fibers project to granule cells mainly by way of mossy fibers and some climbing fibers (for review, see Reference [36]). Granule cell axons split into parallel fibers in the molecular layer (ML) and innervate Purkinje cells (PCs) [37] via thousands of glutamatergic synapses. Outward cerebellar tracts start at PCs, then project to deep cerebellar nuclei (DCN), and leave the cerebellum mainly through the superior peduncles. Notably, both PCs and DCN neurons exhibit dense SMN expression in humans [38,39] and in rats [31]. These efferent fibers from the cerebellum carry signals to the thalamus where they project back to the motor cortex, and the brainstem where they modulate descending inputs to the spinal cord.

Surprisingly, given its critical role in motor refinement, the cerebellum is still one of the least investigated brain regions for defects related to SMA. However, there are a growing number of clinical reports documenting cerebellar pathology in SMA patients. In the cerebellum of severe SMA patients (type 0 and 1), neurodegeneration, neuron ballooning, and neuronophagia [23,27] as well as progressive atrophy [34] have been observed. In another study of type 3 and 4 SMA patients, selective cerebellar degeneration was observed in cerebellar lobules VIIIIB, IX, and X [40]. In our previous work with the *SMNΔ7* mouse model, we found that the intrinsic properties and synaptic transmission of PCs—the sole output neuron of the cerebellar cortex—were significantly affected [41]. These data support the involvement of the cerebellum in SMA pathology.

To fully assess pathology in SMA-affected cerebella and build on our previous work, we investigated the structural, cellular, and functional defects of the cerebellum in the *SMNΔ7* mouse model using magnetic resonance imaging (MRI), immunohistochemistry (IHC), and electrophysiological techniques. Here, we report results from: (i) T2-weighted images from MRI revealing a differential loss in SMA cerebellar volume; (ii) diffusion tensor imaging (DTI) showing that SMA affects the

FIGURE 1 Spinal muscular atrophy (SMA)-affected cerebella were disproportionately smaller and display uniform morphological abnormalities relative to controls. (A) Representative 3D renditions of control and SMA-affected cerebella from manual segmentation of T2-weighted images at P12 (scale bar = 1 mm). (B–D) Volumetric measurements of 3D renditions from segmentations for control and SMA affected. (B) Whole-brains, (C) cerebella, and (D) cerebellar volume as a percentage of whole brain volume were smaller in SMA compared to controls. (E) Point-to-point length measurements of various cerebellar dimensions. Inset: representative cerebella displaying how length measurements were acquired, ⊗ refers to the location of the depth measurements. $**p < 0.01$, $***p < 0.001$ for SMA ($n = 6$) compared to control ($n = 5$), unpaired two-tailed Student's *t*-test.



afferent and efferent cerebellar pathways, as well as intra-cerebellar connections (ICCs); (iii) IHC staining showing structure changes, neurodegeneration, and glia defects in SMA-affected cerebellum; and (iv) electrophysiology recordings from DCN neurons showing that the observed structural and cellular pathology defects impair the functional output of the cerebellum. Using a mouse model to elucidate SMA pathologies in the cerebellum, we expand the understanding of SMA disease mechanisms as more than just a motor neuron disorder, and progress toward developing comprehensive methods for treatment and therapy.

2 | RESULTS

2.1 | Reduced SMN expression levels in SMA-affected cerebella

We performed western blots using dissected brain regions from healthy and mutant SMN Δ 7 at post-natal day 12 (P12) mice for comparison of SMN expression to the spinal cord. The levels of SMN expression in the cerebellum, brainstem, thalamus, and hippocampus of healthy

mouse brains were comparable to the spinal cord. There was no significant difference in SMN expression among the different brain regions of control mice or among different brain regions of SMA mice. When comparing between SMA and control, the cerebellum and spinal cord showed significantly lower SMN expression levels in SMA tissues ($*p < 0.05$). Other regions were nearly significant, with a few outlier data points preventing statistical significance. This included the brainstem as well as cortex 2 ($^{\circ}p = 0.0912$ and $^{\circ}p = 0.0642$, respectively) (Figure S1), which is defined as the cortex caudal to approximately bregma = -0.5 mm. This experiment confirms previous SMN expression level findings in specific brain regions and provided us the rationale to continue with a thorough investigation into SMA pathology in the cerebellum.

2.2 | Cerebellar volume was disproportionately affected in the brains of SMA mice

We initially measured the volume of the brain and cerebellum in SMN Δ 7 mice at P12 to investigate how the

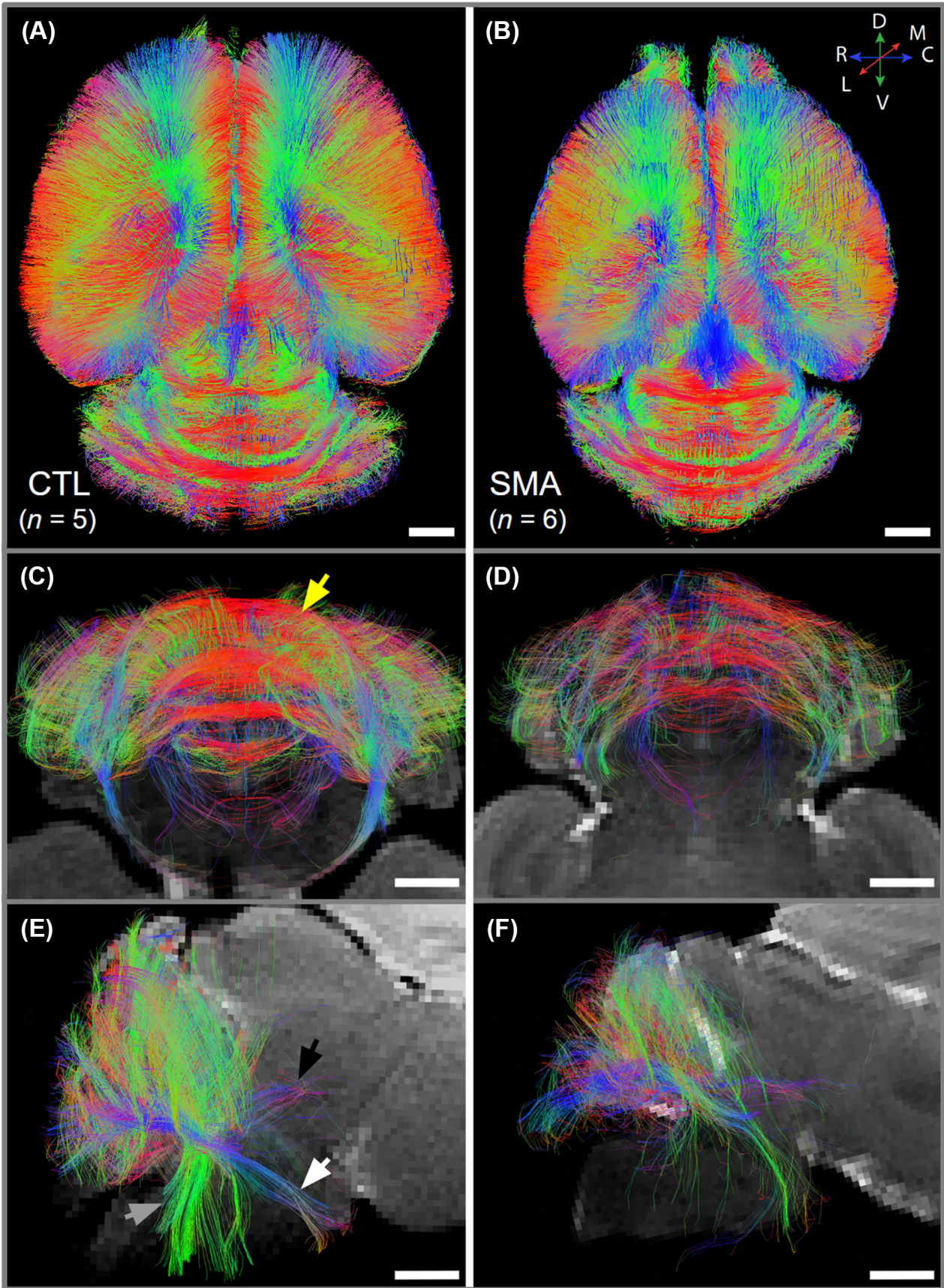


FIGURE 2 Legend on next page.

brain may be affected by SMA. To do this, we used semi-automatic and manual segmentation of T2-weighted images to generate 3D renderings of the brain and cerebellum, respectively (Figure 1A). The whole brain volume was significantly smaller in SMA mice ($n = 6$) as compared to control ($n = 6$) (Figure 1B, see Table S1 for significance tests); the same was observed for SMA cerebella as well (Figure 1C). Importantly, SMA-affected cerebellar volume relative to whole brain volume was also significantly lower compared to control (Figure 1D), indicating that the volume loss for the cerebellum was greater than that for the rest of the brain. We also compared dimension-specific morphology across groups. This included cerebellar width, as well as depth and height measurements for the vermis, left hemisphere, and right hemisphere. The differences in morphology measurements between SMA cerebella and controls were relatively uniform. We also calculated hemisphere ratios to test if volume loss was greater on one side or the other, and found no significant difference between hemispheres across groups (Figure 1E, see Table S1 for significance tests). These results suggest that pathology in the cerebellum manifests symmetrically, which is consistent with the symmetrical muscle weakness observed in SMA patients [9].

2.3 | Cerebellar fiber tracts and diffusivity were significantly different between SMA and control mice

To investigate how cerebellar connectivity is altered in SMA-affected mice, we quantified tract formation between key motor circuit components based on their passage through cerebellar peduncles and within the cerebellar cortex using DTI and probabilistic tractography. Tract reconstruction revealed fewer tracts and less organization of white matter pathways across the brain (Figure 2A,B). Within the cerebellum, many of the ICCs, such as climbing and mossy fibers (green), as well as parallel fibers (red; [42]), were less apparent in SMA compared to control (Figure 2C,D). Most notably, SMA cerebellar input and output pathway formation were largely missing and lacked the same conserved organization as controls (Figure 2E,F). We adapted a previous protocol for diffusion tractography analysis to quantify these observations [43]. For sagittal planes across one half of the cerebellum (Figure 3A), we quantified the

presence of each tract type in each single-voxel regions-of-interest (ROIs; Figure 3B) and compared across groups (Figure 3F–J). In many cases, several tract types were observed in a single voxel ROI.

Superior peduncular tracts (SPTs) were defined as pathways that leave the cerebellum through the superior peduncle and projected into the midbrain. The extent of SPT formation for SMA-affected cerebella was lower within the intermediate zone and vermis, but these differences were not statistically significant (Figure 3C,F). Middle peduncular tracts (MPTs) connect the cerebellum to the pontine nucleus through the middle peduncle and were consistently present across the sagittal planes probed. Notably, there were significantly lower MPTs in the cerebellar hemisphere in SMA versus controls (Figure 3D,G). Inferior peduncular tracts (IPTs) were defined as pathways that leave the cerebellum through the inferior peduncle and mainly descend toward the spinal cord. IPTs were also uncommon in the hemispheres in SMA mice ($>10\%$ of voxels) and increased in the intermediate zone and vermis. Unlike the SPTs, IPT tract formation was significantly diminished in two planes within the vermis of SMA-affected cerebella (Figure 3E,H). Voxel ROIs containing tracts confined within the cerebellum (ICCs) were slightly less common in SMA-affected cerebella (Figure 3I). Furthermore, voxel ROIs tended to have a higher likelihood of no tract formation (NTF) in SMA cerebella (Figure 3J). Significance values for each tract at each mediolateral distance are shown in Table S2. For both ICCs and NTF, trends of less tracts spanned the cerebella. Overall, tract reconstruction is less likely in SMA cerebella, indicating that white matter pathway formation may be weakened by SMN deficiency, most notably in inferior and MPTs. These results suggest that the inputs from the cerebral cortex, brainstem, and spinal cord were significantly altered in SMA mice, whereas outputs through the SPTs were not significantly affected.

To further characterize microstructure within the cerebellum, we acquired sagittal plane ROIs across the entire cerebellum to quantify common diffusivity measurements such as fractional anisotropy (FA), mean diffusivity (MD), axial diffusivity (AD), and radial diffusivity (RD). FA measures the overall directionality of water diffusion and is greater in white matter tracts and lower in extracellular space and disorganized fibers. FA showed little variation within the cerebellar hemispheres but was significantly greater in six sagittal planes

FIGURE 2 Cerebellar tract reconstructions were less organized and peduncular pathway formation was diminished in spinal muscular atrophy (SMA) mice compared to controls. (A,B) Comparison of probabilistic tract reconstructions between representative brains for (A) control and (B) SMA (top panels). Color-coding of tracts represents the average direction as shown in (B). For example, fibers that primarily course from rostral (R) to caudal (C) are in blue. (Middle panel) Cerebellar ROIs isolate tracts within or connected to cerebellum. Axial view of cerebellar pathways shows parallel fibers (in red, yellow arrow), mossy fibers, and climbing fibers (in green). (Bottom panel) Sagittal view of cerebellar pathways shows superior (black arrow), middle (white arrow), and inferior (gray arrow) peduncular tracts. C, caudal; D, dorsal; L, lateral; M, medial; R, rostral; V, ventral. Scale bars = 1 mm.

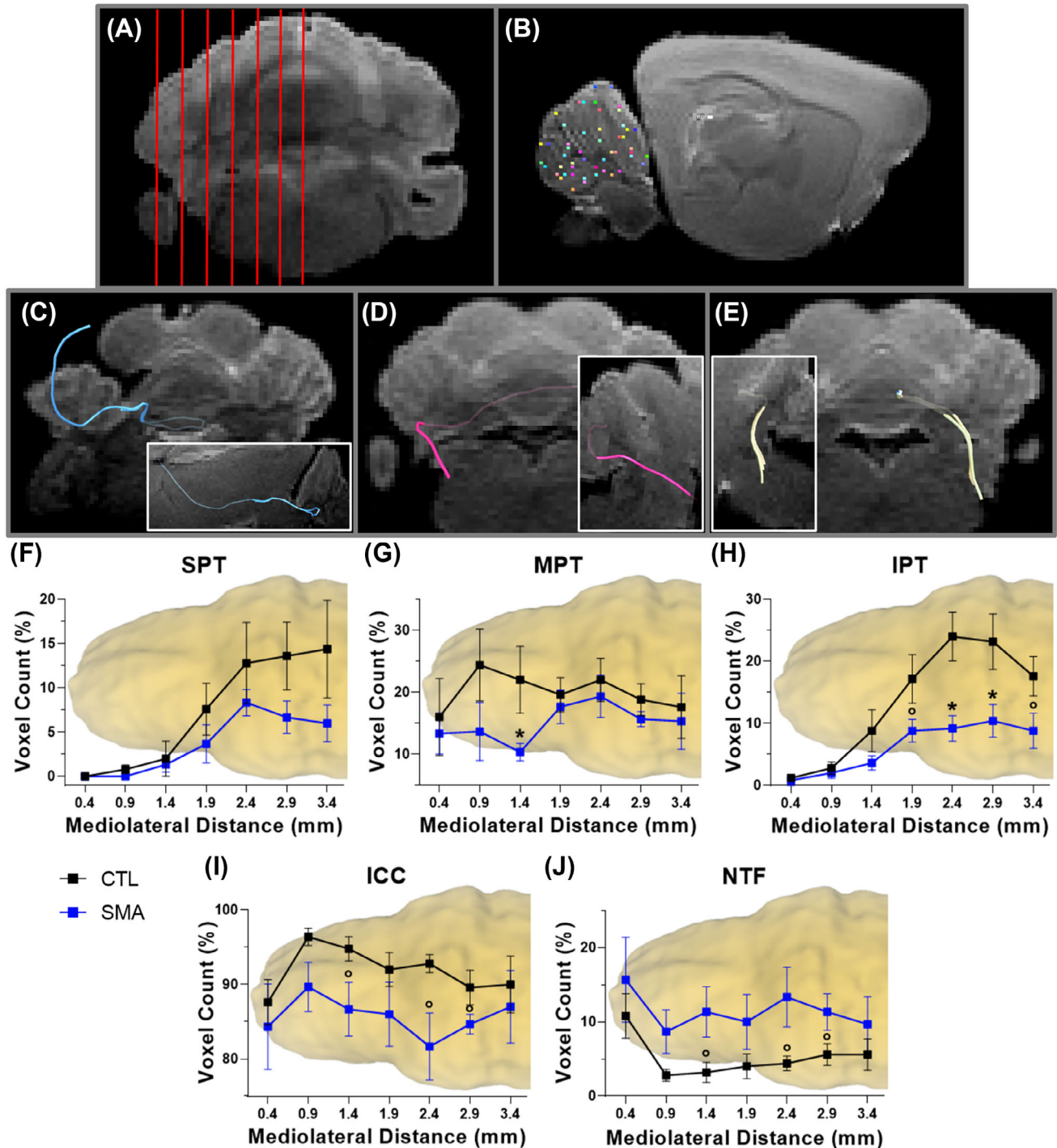


FIGURE 3 Diffusion tractographical analysis revealed that afferent fiber tracts were significantly lower in spinal muscular atrophy (SMA)-affected cerebella relative to controls. (A) Representative coronal T2-weighted image. Red lines represent the sagittal planes probed. (B) Colored boxes indicate a total of 50 randomly selected single-voxel ROIs within each of the sagittal planes of the cerebellum. These were used for quantification of fiber pathways. (C–E) Examples in a control cerebellum of the categorized tract types in coronal T2-weighted images with white matter pathway reconstruction (inset: sagittal view): (C) superior peduncular tract (SPT), (D) middle peduncular tract (MPT), and (E) inferior peduncular tract (IPT). (F–J) Each tract type is quantified as a percentage of all single-voxel ROIs. A coronal view of a representative cerebellum was displayed to help visualize the mediolateral distance. Each point represents the sagittal plane probed and the distance from the lateral edge of the cerebellum. ICC, intra-cerebellar connection; NTF, no tract formation within the single-voxel ROI. $^{\circ}p < 0.10$, $*p < 0.05$ for SMA ($n = 6$) compared to control ($n = 5$), multiple unpaired two-tailed Student's t -test for each tract category.

across the vermis region in SMA-affected cerebella compared to controls (Figure S2A). MD can be affected by any process that alters the barriers that maintain the

directionality of water diffusion, such as cell membranes. MD was generally lower in the SMA cerebella compared to controls; however, the difference was significant for

just 2 sagittal planes (Figure S2B). The combination of higher FA and lower MD in conditions of neuropathology is commonly attributed to edema, inflammation, and microglial activation [44,45].

AD quantifies the magnitude of water diffusion along the principal direction of diffusion and showed a similar trend of lower measurements in SMA cerebella. However, only one sagittal plane in the hemisphere showed significantly lower AD in SMA-affected cerebella relative to controls ($x = 2.6$, $*p < 0.05$; Figure S2C). For RD measurements, there was also an overall trend of lower values, with nine sagittal planes across the vermis and intermediate zones and one sagittal plane in the hemisphere showing statistically significant differences (Figure S2D). While higher RD measurements are generally understood to correlate with demyelination, the contribution of myelination to DTI-derived measures in brain white matter is complex [46], and lower RD measurements might also reflect differences in axonal diameters or density [47]. Taken together, these results suggest diffuse pathology in the cerebellum with certain medio-lateral regions more affected than others.

2.4 | SMA is associated with lobule-specific structural abnormalities and degeneration of PCs

We next investigated defects in the structure and cell types of the cerebellum in SMA mice using IHC staining. To do this, two sagittal slices were stained within the intermediate zone of cerebella using anti-calbindin, and counterstained with hematoxylin (Figure 4A,B). Calbindin is a common marker for PCs because it provides adequate visualization of PCs and surrounding substructures [48]. We investigated PCs across entire slices and found that the number of PCs (Figure 4C) and their area (Figure 4D) were significantly lower in SMA cerebella compared to controls. To quantify the extent of structural abnormalities and PC loss within particular lobules, we acquired area and perimeter measurements, counted the number of PCs, and calculated PC density and PC perimeter density for each lobule, as described in the methods. We observed distinct structural and PC abnormalities within the more posterior lobules of the cerebellum. Specifically, the Ansiform Crus 2 (ANCr2) and paramedian (PRM) lobules were most affected in SMA cerebella. Lobule area was significantly smaller compared to controls in the ANCr2 and PRM lobules (Figure 4E; $*p < 0.05$ for both), and PCs were significantly fewer compared to controls in the PRM lobule ($*p < 0.05$) and close to significance for ANCr2 as well ($p < 0.086$; Figure 4F). Interestingly, the Culmen 4/5 lobule displayed a significantly lesser PC density compared to controls ($*p < 0.05$), while the trend was opposite for the ANCr2 and PRM lobules ($*p < 0.05$ and $p = 0.13$, respectively; Figure 4G). This was the only instance in our analysis where a lobule besides ANCr2 or PRM showed a significant, or near significant, difference

between SMA and controls. Perimeter measurements showed no significant difference for any of the lobules across groups. However, for PC perimeter density, a measurement that reflects the layered nature of PCs in the cerebellum, the SMA cerebella were significantly higher compared to controls in the ANCr2 lobule ($***p < 0.001$) and nearly the PRM lobule ($p = 0.077$; Figure 4H). In our analysis, not all cerebellar cell types exhibited degeneration. For example, neurons within the DCN of SMA cerebella showed no significance in passive membrane properties (Table S3), cell densities or soma areas (Figure S3A–C). These results suggest that there was no neurodegeneration of DCN neurons, but that neurodegeneration is present in the cerebellum in a lobule and cell-type specific manner.

2.5 | SMA cerebella exhibit lobule-specific abnormalities in layer structure and granule cell migration across the ML

The cerebellum is an intricately layered substructure, thus we examined how SMN deficiency may affect the structure of the internal and external granule layers (IGL and EGL, respectively), as well as the PC and ML (PCL + ML). We used Anti-NEUN antibody staining as a marker for granule cells [49], but due to the extremely high density of cells we were unable to accurately analyze granule cell count and degeneration in the IGL and EGL of SMA cerebella. However, we were able to examine cerebellar substructure by measuring the thickness of cerebellar layers within lobules which were among the least (SIM lobule) and most (ANCr2 lobule) affected for SMA cerebella compared to controls (Figure 4D). In the least affected simple (SIM) lobule, thicknesses were generally unchanged except for the EGL being slightly thicker in SMA-affected cerebella than in controls ($*p < 0.05$, Figure 5A–C). Total SIM lobe thickness was nearly identical in both groups (Figure 5D). Interestingly, the greatest discrepancies were observed in posterior lobes, which also had the most lobule and PC defects in SMA cerebella. The IGL, PC + ML, and external granule layer thicknesses were all significantly thinner in SMA posterior lobes relative to controls. Within the posterior lobes, the internal granule layer thickness was approximately 25% thinner ($***p < 0.01$), the PC and ML thickness was approximately 45% thinner ($***p < 0.0001$), and the external granule layers thickness was approximately 76% thinner ($***p < 0.0001$) in SMA-affected cerebella compared to controls (Figure 5E–G). The total posterior lobule thickness of SMA-affected cerebella was significantly lesser than in controls ($***p < 0.0001$, Figure 5H), providing some context to earlier findings of cerebellar volumetric loss.

In the early postnatal period in mice, post-mitotic granule cells migrate across the ML after proliferation from the external granule layer to the internal granule layer (Figure 5I; [50]). We observed that the density of

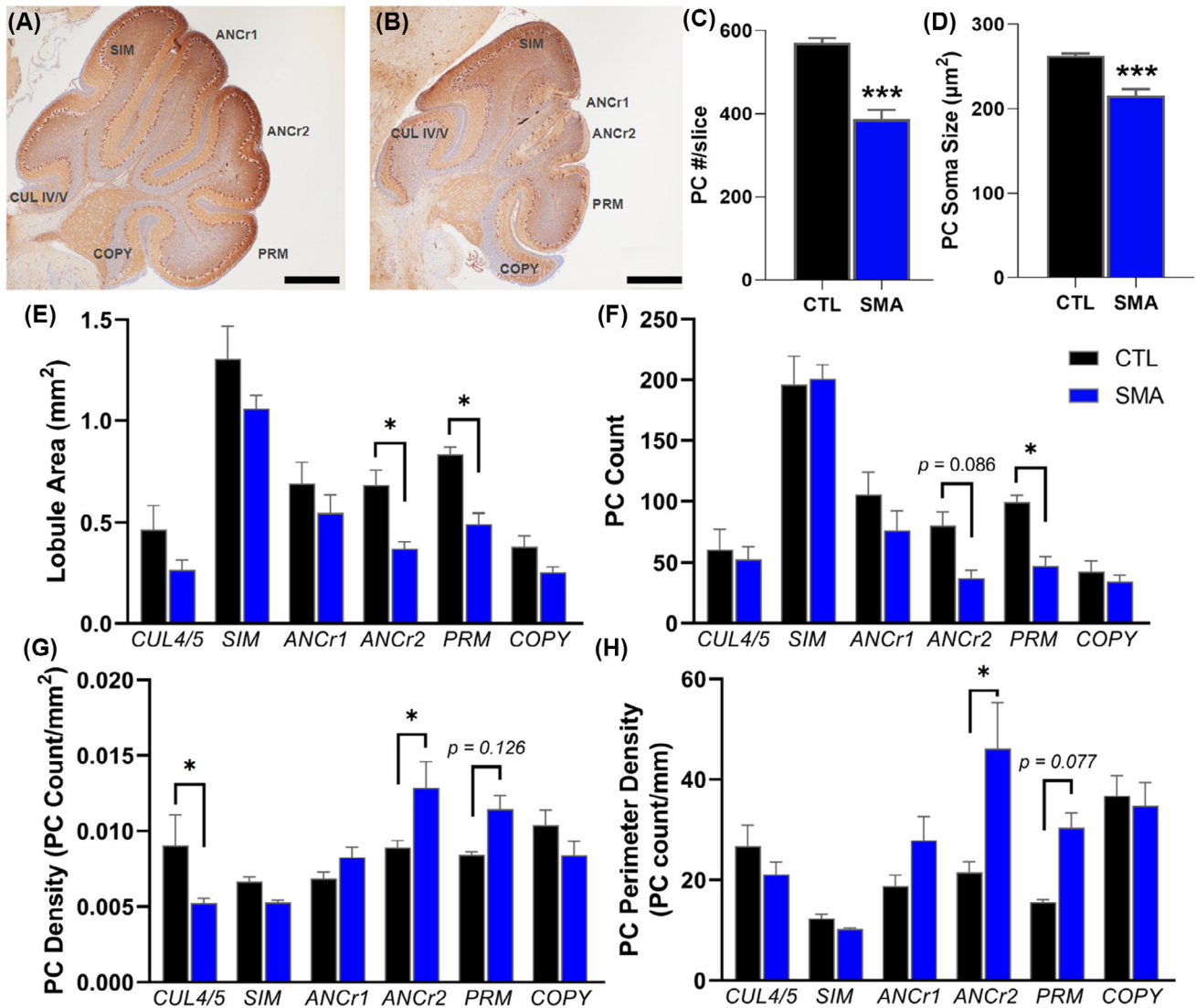


FIGURE 4 Spinal muscular atrophy (SMA)-affected cerebella displayed structural abnormalities and Purkinje cell (PC) neurodegeneration localized to the posterior lobules. Representative anti-calbindin stained images with labeled lobules for (A) control and (B) SMA cerebella. Scale bar = 1 mm. (C) Average number of PCs detected per stained slice was less in SMA compared to control. (D) PC soma size quantified by area was smaller in SMA compared to control. (E) Lobule area was significantly smaller for the ANCr2 and PRM lobules in SMA cerebella. (F) PC count was significantly lower in the PRM lobule. (G) PC density, as measured by PC number divided by lobule area, was significantly lower for the CUL 4/5 lobule and higher for the ANCr2 lobule. (H) PC perimeter density, as measured by PC number divided by the perimeter, was significantly higher for the ANCr2 lobule. Comparisons with near significant p -values are shown. Lobules: CUL IV/V = culmen 4/5; SIM = simple; PRM = paramedian; COPY = copula pyramidis. * $p < 0.05$, ** $p < 0.01$, *** $p < 0.001$ for SMA compared to control ($n = 12$ slices, $n = 6$ mice for both control and SMA), (C,D) unpaired two-tailed Student's t -test, (E–H) ordinary one-way ANOVA with Šidák's multiple comparisons test.

migrating granule cells was higher in SMA-affected cerebella for both the least and most affected lobules compared to controls (SIM; * $p < 0.05$ and ANCr2; ** $p < 0.01$, respectively; Figure 5J,K), suggesting that the migration of granule cells in the cerebellum may be slowed in SMA mice. The lobule-specific differences in the thickness of cerebellar layers suggest structural abnormalities in the posterior lobes of P12 SMA mice. However, the fact that immature migrating granule cell density in the ML was greater for both the least affected and most affected lobules in SMA mice relative to controls suggests that SMN deficiency is associated with

changes in the migratory behavior of granule cells across the entire cerebellum.

2.6 | Astrocyte integrity is affected in cerebellar peduncles and in cerebellar gray and white matter

Glial cells have been suggested to play a critical role in the development of motor neuron dysfunction in SMA [51], and astrogliosis has been reported in SMA mice and patients [52]. Thus, we investigated how astrocyte

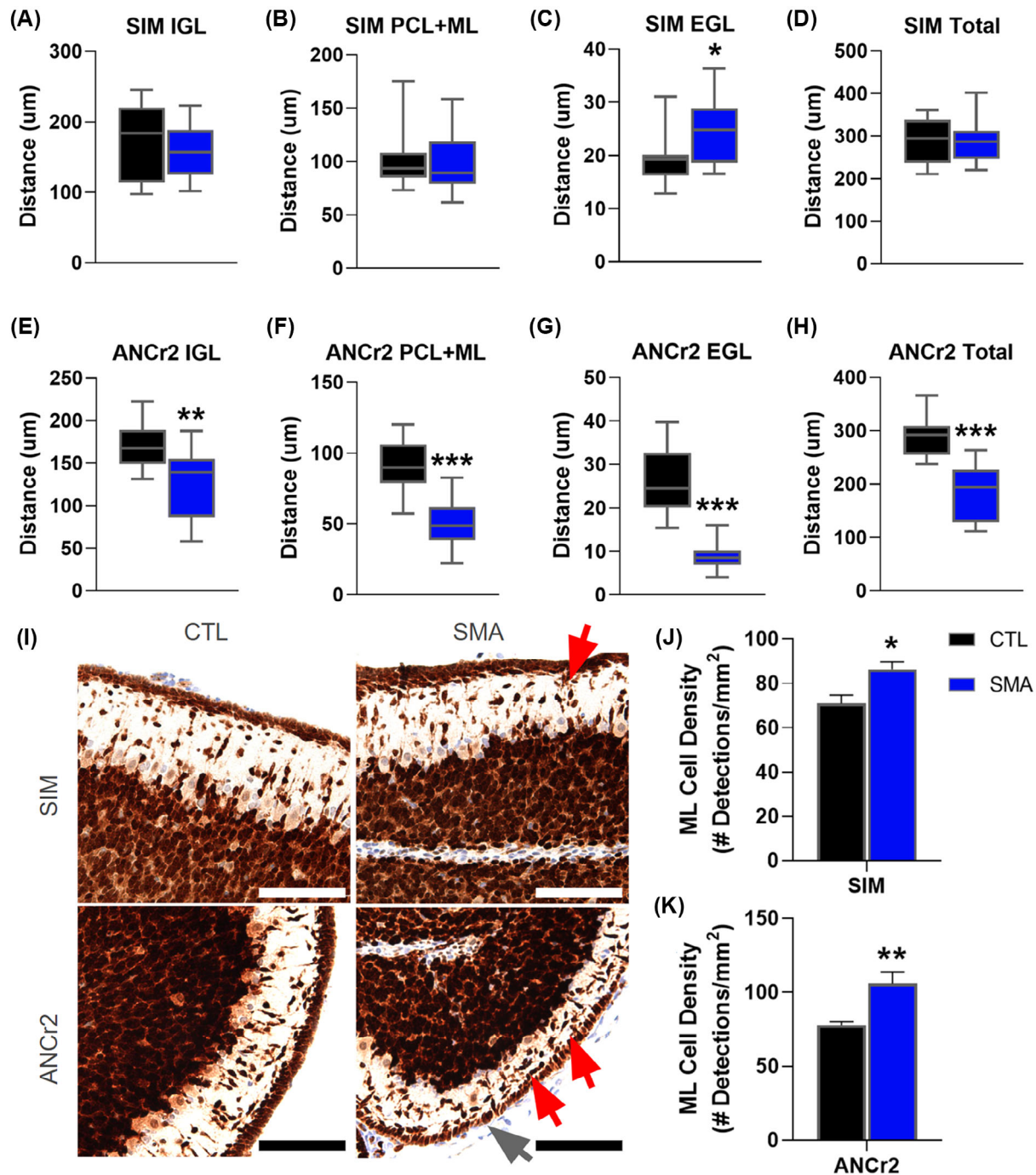


FIGURE 5 Cerebellar layers in posterior lobes, such as ANCr1 and ANCr2, were thinner in spinal muscular atrophy (SMA) mice compared to controls, with a higher density of migrating granule cells in the ML. Cerebellar layer thickness was measured in microns (y-axis) at three locations for each cerebellar layer and averaged to compare between SMA ($n = 12$) and control ($n = 12$) cerebella (A–H). Comparisons between SMA and control were made in the less affected simple (SIM) lobule (A–D) and the more affected posterior lobules (E–H). (A,E) Internal granule cell (IGL), (B,F) Purkinje cell and molecular (PCL + ML), (C,G) external granule cell (EGL), and (D,H) total thicknesses (measured from the outer edge of the arbor vitae to the crown). (I) Images of representative Anti-NeuN stained slices of the ML in the SIM and ANCr2 lobules for control and SMA cerebella. Red arrows point to areas of increased granule cell density for both the (J) SIM and (K) ANCr2 lobules. The gray arrow points to the thinner EGL of the SMA ANCr2 lobule. * $p < 0.05$, ** $p < 0.01$, *** $p < 0.001$ for SMA compared to control ($n = 12$ slices, $n = 6$ mice for both SMA and control), unpaired two-tailed Student's t -test. Scale bars = 100 microns.

integrity was affected in the cerebella of $SMN\Delta 7$ mice using Anti-GFAP antibody staining in the white matter (Figure 6) and gray matter regions (Figure 7). We assessed astrocyte integrity by quantifying stain intensity using optical density and positive pixels per μm^2 for the cerebellar regions of interest (ROIs). Comparisons were

made between SMA lobules and control lobules, as well as between what we define as posterior lobules (ANCr1 and ANCr2) and anterior lobules (SIM and CUL 4/5) within SMA brains. In the *arbor vitae* branches of the anterior cerebellar lobules, the GFAP optical density of SMA cerebella was significantly lower compared to that of control

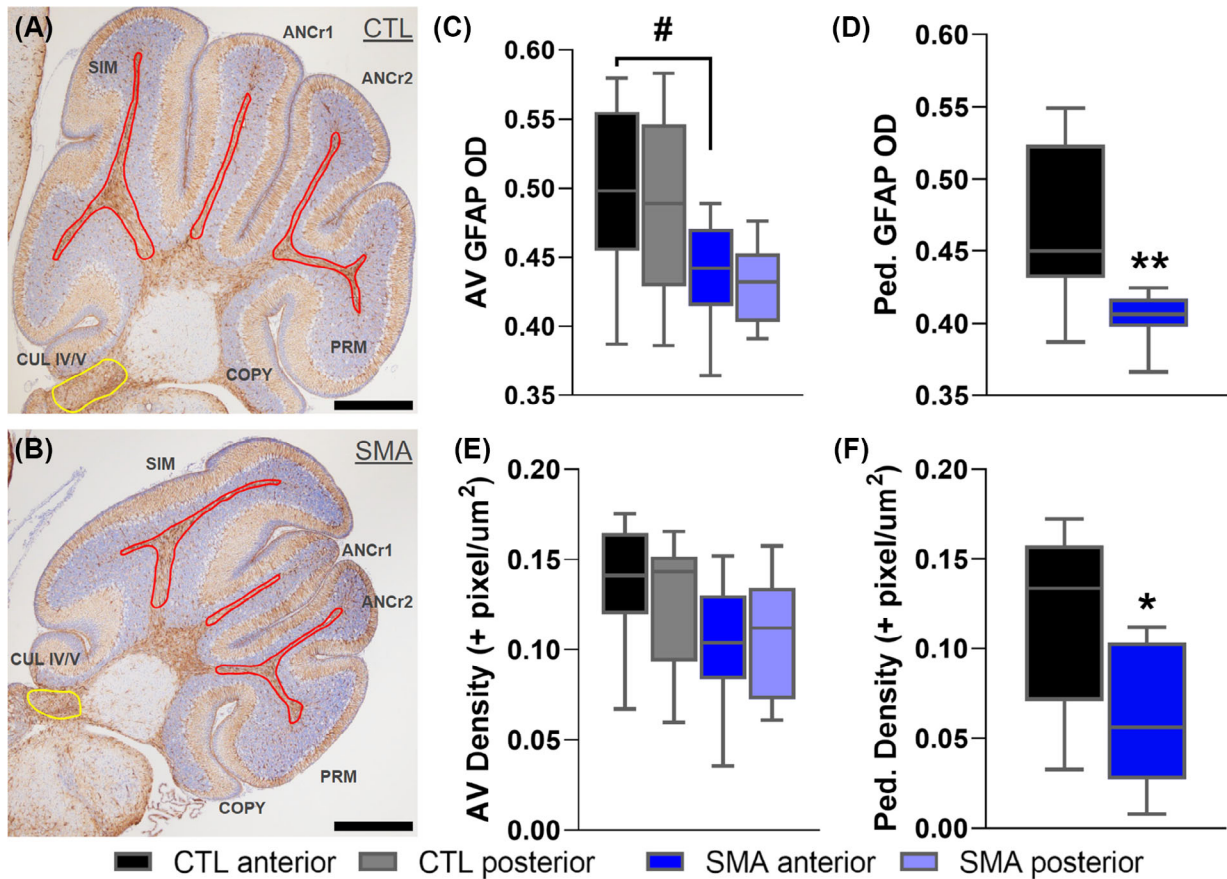


FIGURE 6 Glial cell structural integrity was lower in white matter regions. Representative Anti-GFAP stained slices for (A) control and (B) spinal muscular atrophy (SMA) cerebella with each lobule labeled. Sample ROIs are drawn for the arbor vitae (red) and cerebellar peduncles (yellow). (C) GFAP optical density and (E) GFAP positive pixel per μm^2 measurements for arbor vitae (AV) of the control and SMA anterior and posterior lobules. (D) GFAP optical density and (F) GFAP positive pixel per μm^2 measurements for the control and SMA-affected cerebellar peduncles. $^{\#}p < 0.05$ for SMA anterior lobules compared to control anterior lobules, $^*p < 0.05$, $^{**}p < 0.01$ for SMA ($n = 12$ slices, $n = 6$ mice) compared to control ($n = 12$ slices, $n = 6$ mice), (C,E) Ordinary one-way ANOVA with Tukey's multiple comparisons test, (D,F) unpaired two-tailed Student's t -test.

cerebella ($^{\#}p < 0.05$). The optical density of GFAP in the *arbor vitae* of the posterior cerebellar lobules trended lower in SMA cerebella compared to control ($p = 0.0518$; Figure 6C). GFAP staining between posterior and anterior lobules within SMA cerebella was similar for measurements of both GFAP optical density ($p = 0.9797$) and pixel density ($p = 0.9916$). Within the peduncles, both GFAP optical density and positive pixels per μm^2 were significantly lower in SMA cerebella compared to controls ($^{**}p < 0.01$ and $^*p < 0.05$, respectively) (Figure 6D,F). These results are consistent with the indication of fiber tract abnormalities observed in SMA cerebella in our DTI tractography data.

After assessing astrocyte integrity in cerebellar white matter, we investigated it in cerebellar gray matter. GFAP optical density was acquired and positive pixels per μm^2 was calculated in the ML, IGL, and DCN (Figure 7A,B). The ML of posterior lobules in SMA-affected cerebella exhibited greater GFAP optical density relative to the control counterparts ($^{##}p < 0.01$) and to the unaffected anterior lobes of SMA cerebella (Figure 7C; $^{***}p < 0.001$). GFAP positive pixel density was significantly greater in both comparisons as well (Figure 7F; $^{\#}p < 0.05$ and $^{***}p < 0.001$, respectively). The IGL of posterior lobes in SMA-affected

cerebella displayed greater GFAP positive pixel densities compared to both posterior lobes of control cerebella ($^{####}p < 0.001$) and anterior lobes of SMA-affected cerebella ($^{***}p < 0.001$). These differences were extreme, at 4.5 times greater and 7 times greater than controls, respectively (Figure 7D,G). This data suggested activated astrocytes and reactive gliosis in SMA-affected cerebellar gray matter. Although DCN neurons did not display degeneration (Figure S3), activated astrocytes and reactive gliosis were also observed in this region. DCN glial cells displayed 7-fold greater positive pixel density in SMA-affected cerebella as compared to control ($^{**}p < 0.01$, Figure 7H). These data suggest that in SMA-affected cerebella, the significantly higher GFAP expression in the more posterior lobules may be an astrocytic response to the PC degeneration observed in these regions.

2.7 | Output neurons in the DCN of SMA mice display abnormal functional output

Having assessed fiber pathway structure and cellular pathology, we aimed to investigate the functional output

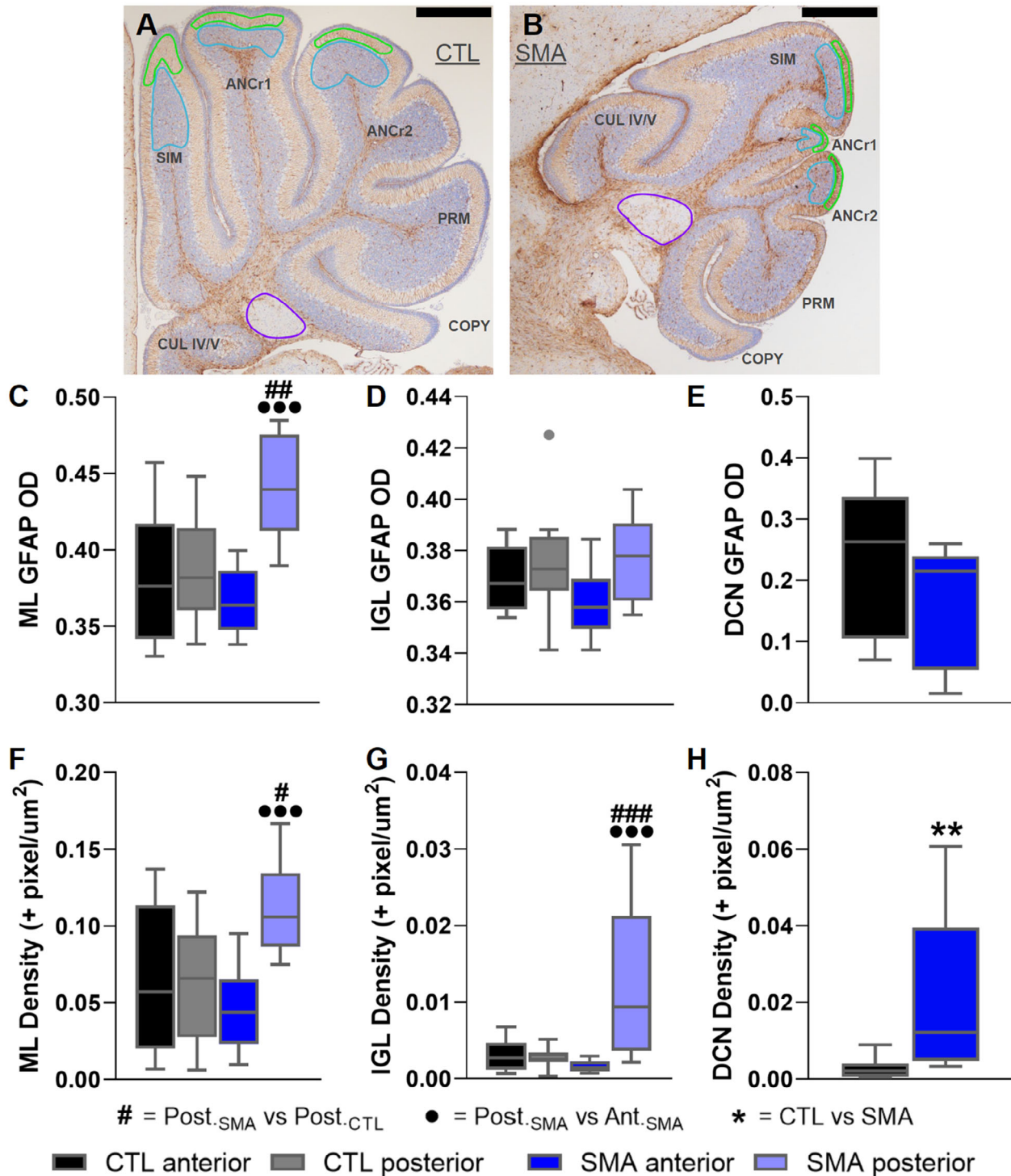


FIGURE 7 Reactive gliosis was observed in the gray matter of the cerebellum, such as the molecular and internal granular layers of posterior lobes, as well as the deep cerebellar nuclei (DCN). Representative Anti-GFAP stained images for (A) control and (B) spinal muscular atrophy (SMA)-affected cerebella with each lobule labeled. Sample ROIs are drawn for the internal granule layer (IGL, cyan), molecular layer (ML, green), and DCN (purple). GFAP optical density for the (C) molecular layer (ML), (D) internal granule cell layer (IGL), and (E) DCN. GFAP positive pixel per μm^2 for (F) the ML, (G) the IGL, and (H) the DCN. * $p < 0.05$ control versus SMA, *** $p < 0.001$ posterior SMA lobules ($n = 12$ slices, $n = 6$ mice) versus anterior SMA lobules ($n = 12$ slices, $n = 6$ mice), # $p < 0.05$, ## $p < 0.01$, ### $p < 0.001$ posterior control lobule ($n = 12$). (C,D,F,G) ordinary one-way ANOVA with Tukey's multiple comparisons test, (E,H) unpaired two-tailed Student's t -test. Scale bar = 500 microns.

of the cerebellum by measuring the spontaneous firing and intrinsic properties of the output neurons of the DCN. Only neurons with greater than 20 μm soma

diameter, complex dendritic branches, spontaneous firing, and less than 500 ms rebound depolarization that are characteristic of DCN output neurons were included in

the analysis. These are signature characteristics of the glutamatergic output neurons that we intended to study [53]. Among these output neurons, 100% showed spontaneous firing in control cerebella (three animals, $n = 11$ cells), while only 58.8% showed spontaneous firing in SMA cerebella (three animals, $n = 17$ cells). For DCN neurons from SMA mice, spontaneous firing frequency was only half as much as in DCN neurons from control mice ($*p < 0.05$, Figure 8A,C,D). However, there appeared to be a compensatory effect for evoked action potential firing, with the frequency-current (F-I) measurements suggesting that the SMA cells were more excitable than controls. DCN neurons from SMA mice displayed a steeper increase in action potential firing frequency in response to injected current than DCN neurons from control mice. For current injections between 160 and 300 pA, the neuronal firing frequencies for SMA neurons compared to controls trended toward significance ($0.05 < p < 0.1$) (Figure 8B,E), while the neuronal gain values calculated from the F-I slope were significantly larger in SMA neurons compared to controls ($*p < 0.05$, Figure 8F). We observed no other passive membrane and action potential properties with a significant difference between SMA and control neurons. These measurements included: rheobase current, peak amplitude, threshold,

half-width, after-depolarization potential (ADP) and after-hyperpolarization potential (AHP) for action potential properties, and input resistance, capacitance and time constant for the passive membrane properties (Table S3). These results suggest that the functional output from the DCN is lower in SMA cerebella compared to controls. Interestingly, the excitability of the DCN neurons from SMA mice was increased, which may represent a compensatory response similar to what has been reported for motor neurons [54] and cerebellar PCs [41] from SMN Δ 7 mice.

3 | DISCUSSION

The data presented in this study provide for the first time a comprehensive investigation into cerebellar defects related to reduced functional SMN protein levels. Using the SMN Δ 7 mouse model, we employed a multimodal approach to comparatively identify and characterize pathophysiology in the cerebellum, including MRI with T2-weighted and DT images, histology, and electrophysiology. Recent SMA research supports the notion that SMN is a multi-system disease that uniquely affects cell types beyond spinal cord motor neurons. Our findings in this study strongly support

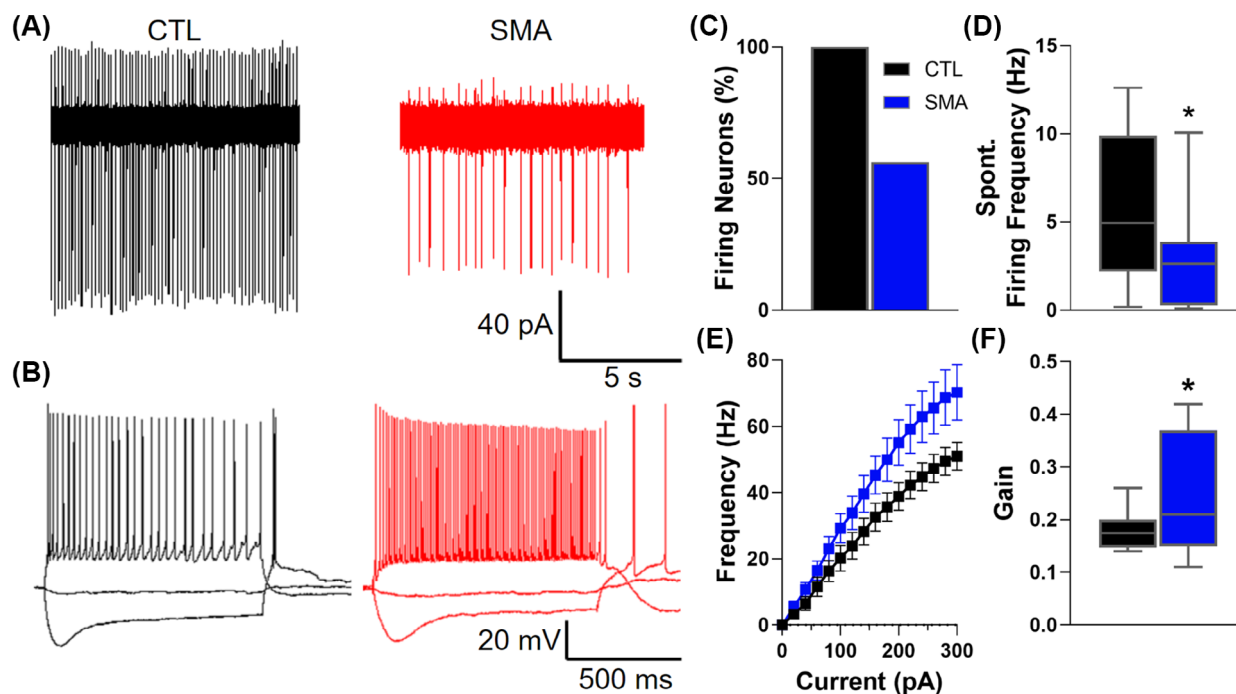


FIGURE 8 Spinal muscular atrophy (SMA)-affected Deep cerebellar nuclei (DCNs) exhibited fewer neurons with spontaneous firing, lower frequency of spontaneous firing, but greater firing frequency in response to current injections. Representative traces of (A) spontaneous firing and (B) evoked action potentials for control and SMA DCN neurons. (C) The percentage of neurons that spontaneously fired during cell-attached measurements for control ($n = 11/11$) and SMA ($n = 10/17$). (D) Spontaneous firing frequency for control ($n = 11$) and SMA ($n = 10$) DCN neurons. (E) Frequency-current (F-I) relationship for evoked action potential firing for control ($n = 10$) and SMA ($n = 11$). (F) Neuronal gain values calculated from the F-I slope. $*p < 0.05$ for SMA compared to control, (D,F) unpaired two-tailed Student's t -test, (E) multiple unpaired one-tailed Student's t -test with Welch correction.

this conception of SMA. The observed pathologies show that cerebellar dysfunction may contribute to SMA pathogenesis, and that SMN function is essential to the development, function, and health of specific cerebellar cell types.

3.1 | Disproportionate loss in SMA cerebella volume

Volumetric segmentation revealed that SMA-affected brains display significantly lower volumes in both the whole brain and the cerebellum. A smaller brain is consistent with reported differences in body mass for SMN Δ 7 mice at about P12 [55]. However, we found that cerebellar volume as a percentage of whole brain volume was significantly lower as well, indicating that the cerebellum experiences a greater reduction of volume due to SMA than the rest of the brain. Although causes for smaller brain size are complex and difficult to isolate, we propose that this could be attributed to a combination of three factors: (1) abnormal motor usage and subsequent reduction in functional communication to the cerebellum, a result of spinal cord motor neuron degeneration, (2) loss of white matter tracts, which our DTI analysis provides evidence for, and (3) neurodegeneration of cell types that are particularly reliant on normal SMN function, and our western blot and IHC analyses provide evidence for that. Pertaining to the neuromuscular dysfunction, SMN Δ 7 mice display hind limb fibrillation and abnormal gait [55] that leads to reduced electrical output and muscle innervation from those areas [56,57]. A similar reduction has also been observed in humans with correlation to SMN2 copy number [58,59]. Humans that experience limb amputation [60] and spinocerebellar ataxias [61–64] have been shown to experience losses in cerebellar volume, indicating that reduced functional motor communication may lead to reduced cerebellar volume. In addition, SMA cerebella exhibited less tract formation in our DTI analysis, and white matter makes up a significant portion of cortical volume [65].

The role of neurodegeneration in the smaller size of SMA cerebella is complicated by the array of defects we observed in response to SMA. Loss of PCs and abnormal Bergmann glial cells were observed in this study, both of which are essential for proper spatiotemporal foliation of the cerebellum [66]. Additionally, the lobule-specific structural abnormalities that were observed in this study suggest that developmental foliation is affected by SMA, and this could be another contributor to losses in volume. The specific causes for the phenological alterations are difficult to isolate due to the vast functionality of SMN. Nonetheless, the significantly lower SMN levels in the cerebellum and disproportionate losses in volume compared to the rest of the brain provide a rationale for the investigation into SMA pathology of various cerebellar cell types performed in this study.

3.2 | Disruption of cerebellar input pathways in SMA brains

Using DTI, we investigated the integrity of white matter input and output pathways that traverse the cerebellar peduncles, as well as ICCs. This revealed lower fiber tract formation across all tract categories of SMA-affected cerebella, with significant reductions being observed in IPTs and MPTs. The relationship between tractography abnormalities and axonal health and myelination is well documented (for review, see Reference [67]), and hindered axonal outgrowth due to depleted SMN protein may explain this overall trend. This would be consistent with the disruptions observed in axonal outgrowth as a result of SMN depletion in mouse [68,69] and cell culture models of SMA [68–72].

More specifically, we observed large decreases in fiber tract formation in the IPTs. These tracts mostly consist of dorsal spinocerebellar tracts (dSCTs) and tracts from the inferior olivary nuclei that transmit proprioceptive sensory information from Golgi tendon organs and muscle spindles in the trunk and lower limbs [73], the muscles where SMN Δ 7 mice typically exhibit the most severe phenotypes [55]. Reduced IPT formation suggests defects in sensory fibers that project to the cerebellum and is supported by studies in SMA patients and animal models. Clinical studies have shown that SMA type I patients exhibit severe sensory-motor neuropathy [74] and abnormal sensory signal conduction in sural nerves [75]. In sensory neurons cultured from severe mouse models of SMA, abnormal neurite outgrowth and growth cone morphology has also been observed [76]. Additionally, in SMA mouse models, sensory neurons are smaller [77] and show reduced vGlut1-positive synapses in lumbar vertebrae (L) 1 [78] and L3-5 [79], as well as a greater reduction in synaptic transmission [78]. These data describe sensory neurons at sensorimotor synapses within the lumbar regions of mice spinal cords. However, our data suggest that SMN dysfunction affects not only sensory axons that synapse to motor neurons in the anterior horn but all proprioceptive sensory axons, including those that furcate to synapses at Clarke's nucleus. We offer two potential explanations for reduced IPT tract formation: (i) Sensory-motor synapses may be relaying abnormal chemical and electrical signals that subsequently lead to retrograde degeneration or weakening of the second order dSCT sensory axons; and/or (ii) reductions of SMN protein levels in proprioceptive neurons may disrupt axonal outgrowth of second order dSCT sensory neurons during development.

In our diffusion tensor tractography, tracts classified as MPTs are synonymous with pontocerebellar tracts, and are established during development [80]. The area where we observed a significant decrease in the occurrence of MPTs was in the cerebellar hemisphere just outside the intermediate zone. Building on a study in mice that mapped pontocerebellar projections into cerebellar

lobules [81], our findings suggest that defective tracts may originate from the central or caudal pontine nuclei, which are established in development [80] and contain pontine nuclei projections from the temporal and frontal cortices [82]. Interestingly, tracing studies in non-human primates [83,84], as well as functional and structural studies in humans [85–88] have identified bidirectional connections between the prefrontal cortex and Crus I–II lobes of the cerebellum. The same bidirectional connection has been identified in humans using functional MRI [89–92], tractography [93], and dynamic causal modeling [94] between the temporal lobe and Crus I–II lobes. We observed the highest degree of structural and PC degeneration of SMN Δ 7 mice in Ansiform Crus I–II lobules, which may correspond to decreased connectivity with prefrontal or temporal cortices. Several studies suggest that ponto-cerebellar projections, especially to Crus I and II lobules are relevant in executive, language, and spatial function [87,88,95]. Moreover, there is clinical evidence for cognitive and linguistic defects in SMA patients (for review, see Reference [17]). More investigation into basic cerebellar and cerebral mechanisms will help reveal the role of executive, language, and sensorimotor circuitries in the context of SMA. Cortico-ponto-cerebellar pathways are the major input pathway into the cerebellum and link cortical regions with the cerebellum for the coordination and refinement of movement [96]. The observed decrease in MPT formation in our study supports the supposition that cortico-ponto-cerebellar pathways may be experiencing cell-autonomous defects due to lower SMN levels, and that this may be contributing to motor dysfunction in SMA patients.

We also observed higher FA and lower RD along the vermis region of the cerebellum, suggesting restricted water diffusion perpendicular to the principal direction of diffusion [97,98]. Selective neurodegeneration of isotropic cells such as glia in the white matter regions of the cerebellum may be contributing to this effect [99–101], but a deeper investigation into diffusivity metrics including a distinction between cerebellar subregions will be necessary to further elucidate microstructural defects in SMA.

3.3 | Selective neuronal degeneration of PCs in SMA cerebella

PCs have proven widely relevant in neurological conditions such as ataxia, Huntington's disease, and autism spectrum disorder due to their critical role in modulating cerebellar circuitry development (for review, see Reference [102]). However, PCs have been largely overlooked in SMA research [17] even though SMA patients experience neuronal loss [103–105] and PCs in SMA mouse models have displayed distinct functional abnormalities [41]. Spinal cord motor neurons are well studied in SMA, and have consistently exhibited selective vulnerability and neurodegeneration in SMA due to diminished SMN

levels [35] while surrounding cell types remain relatively unaffected [11,26]. Motor neurons express lower levels of full length SMN from the *SMN2* gene than that of surrounding types because of a negative feedback loop between decreased snRNP levels and exon 7 splicing [15,106]. Here, we document a selective degeneration of PCs similar to that of motor neurons, and we suggest that this may be caused by a specific vulnerability resulting from decreased SMN levels. Moreover, PCs are a cell type that strongly express both SMN [38,39,107], and critical apoptotic proteins Bcl-x [21] and NAIP [108,109]. Thus, a deeper investigation relating changes in SMN levels in PCs to their viability may clarify the causes of their vulnerability to degeneration in SMA.

In the cerebellar hemispheres, we observed abnormal lobule structure and PC formation in the posterior lobules of the cerebellum: Ansiform Crus II and paramedian (ANCr2 and PRM, respectively). Posterior lobules were significantly smaller, and PCs were fewer for SMA cerebella compared to controls. This suggests that PC neurodegeneration may contribute to structural abnormalities. However, PC density was higher for these lobules as well. Furthermore, the PC perimeter density, a unique measurement that more accurately represents PC presence in each lobule because of the pseudo-parallelity of PCs with foliation, was increased for these posterior lobules as well. This suggests that there are other factors that contribute to diminished lobule size in SMA cerebella. In spinocerebellar ataxia, patients exhibit atrophy in the posterior lobules of the cerebellar hemispheres as well [110], implying that the atrophic aspect of the hindlimb deficiencies experienced by SMN Δ 7 [111] may be a contributor to this loss in area, or volume.

PCs employ apoptotic mechanisms at the cerebellar midline and along the rostrocaudal axis in a lobule-specific pattern during development [112]. Studies in mouse models and patient tissues have shown that anti-apoptotic and pro-survival pathways are affected by reduced SMN protein levels, and disruptions in the balance of apoptotic mechanisms plays an important role in SMA pathology (for review, see Reference [113]). SMN interacts with proteins in the Bcl-x family to prevent apoptosis, as seen in yeast cells [114], several compartments of mammalian cells [115], and neuroblastoma cells [116]. Reductions in SMN expression levels occur concurrently with reductions in what are normally dense Bcl-2 expression levels [117]; this has been observed in spinal motor neurons of both SMA patients [21,118] and SMA mouse models [119]. Additionally, Bcl-2 proteins are critical in inhibiting Bax-mediated apoptosis [120–122], and knocking out *Bax* in spinal cord motor neurons lessens disease severity in SMA mice [123]. Motor neurons of SMA patients also display longer than normal periods of apoptosis [124,125]. In mice, the number of apoptotic PCs is typically highest in the first post-natal week [112]. Therefore, these observations of PC abnormalities made at P12 may be an indicator that PC degeneration is related to

disruptions in the balance of pro- and anti-apoptotic mechanisms which extends the period of apoptosis in a manner similar to what has been observed in spinal cord motor neurons. These stained slices were within the cerebellar hemispheres, and a deeper investigation into the vermis region as well will aid in clarifying the effect of SMA on PC apoptosis.

3.4 | Astrocytic reaction in SMA cerebella

We found greater glial fibrillary acidic protein (GFAP) stain density in the ML, IGL and DCN of cerebella from SMA-affected mice. We used GFAP staining because its expression levels are a reliable marker of glial response to stress or injury in the CNS [126–129]. Increases in GFAP staining density can be attributed to gliosis, which involves excessive neuronal ballooning, proliferation, and secretion of pro- and anti-inflammatory cytokines [130–133]. Gliosis is a protective mechanism, but in disease or severe injury scenarios can cause a disruption in neurotrophic support, synaptic pruning, and apoptotic balances that can lead to neurodegeneration of neighboring cells [132,133]. In type II and type III SMA patients, gliosis has been observed surrounding degenerating spinal cord motor neurons (MNs) and displays a strong correlation to MN number [21,103]. The same is observed in the spinal cord and brainstem of SMA type I patients, with cytokine increases also documented surrounding degenerating spinal cord MNs [134]. In astrocytes from the spinal cord of SMN Δ 7 mice and from SMA stem cells, increased GFAP expression and decreased expression of an anti-apoptotic marker were observed long before spinal cord motor neuron degeneration [135], suggesting that astrocytic dysfunction occurs as a direct response to SMN deficiency. In our SMA mice, higher stain density in the ML and IGLs was only evident in the posterior cerebellar lobules of the hemispheres, which include ANCr1, ANCr2, and PRM; the same lobules where we also observed PC loss and structural degeneration. Therefore, our data suggest that SMN deficiency in Bergmann cells, the astrocytes that surround PCs in the cerebellum [136,137], may accelerate PC neurodegeneration by disrupting the balance of apoptotic mechanisms in PC somas and their axons that constitute a portion of efferent white matter pathways.

We also observed increased migrating granule cell density in the ML of SMA cerebella, where GFAP staining intensity was also significantly higher. The SMN-deficient Bergmann glia of the cerebellar ML may be imparting disruptions in the granule cell proliferation (GCP) and migration processes as well. It has long been established that PCs and Bergmann cells help to mediate GCP through expression of proteins such as sonic hedgehog [138,139]. The degenerative relationship between PCs and surrounding Bergmann cells may interrupt

mechanisms regulating the development of granule cells. We also found that the average thicknesses of the EGL, IGL, and PC + ML were all significantly lower in the same posterior lobules that displayed pathology for PCs and for glial cells. Thus, we propose that these uniform and lobule-specific reductions in the cerebellum are related to the imbalanced relationship between PCs and glial cells. Additionally, the lobule-dependent effects observed in this study suggest that glial cell expression patterns as well as PC zones of expression [140] may be important in the progression of SMA pathology.

Glial cells in cerebellar white matter, including the *arbor vitae* branches of the cerebellum and the cerebellar peduncles, mainly consist of fibrous astrocytes [137], and SMA mice exhibit lower levels of GFAP staining compared to controls. Decreased GFAP staining levels in the *arbor vitae* and peduncles suggests that these fibrous astrocytes have decreased structural integrity. Given the vast functionality of cerebellar astrocytes, we suspect that many factors may contribute to the lower GFAP stain density we observed. Interestingly, for the *arbor vitae*, this decrease was only observed in posterior lobules, such as the ANCr1, ANCr2, and PRM lobules, further suggesting a relationship between astrocytic integrity and PC degeneration. Decreased GFAP staining in cerebellar white matter may also reflect the health of myelinating glial cells, such as oligodendrocytes [141,142] and may therefore disrupt normal axon formation and be partly responsible for decreased white matter tract formation in SMA. More investigation into the glial cells of the cerebellum will help to elucidate a precise answer to an open question in SMA research: is SMA primarily a neuroinflammatory disease [51,137]? Investigating specific populations using markers for glial cells such as oligodendrocytes and macrophages will be instrumental in developing our understanding of neuroinflammation caused by SMA across the CNS.

3.5 | Disrupted output from SMA DCN

The glutamatergic DCN neurons make up the sole output of the cerebellum, and receive inputs not only from inhibitory PC axons, but also from the collateral projections of mossy fibers and climbing fibers, all of which contribute to the control of cerebellar output [143,144]. In our cell-attached electrophysiological recordings of DCN output neurons, we found striking differences between SMA and control. SMA DCN neurons were about half as likely to exhibit spontaneous firing compared to control DCN neurons. When SMA DCN neurons did spontaneously fire, the firing frequency was half the speed of control DCN neurons. Interestingly, the excitability for the neuronal gain of SMA DCN neurons was higher compared to control, as suggested by the frequency-current relationship in Figure 7E,F. Recently,

we reported that the spontaneous inhibitory synaptic activity in PCs was lower in SMA cerebella compared to controls [41]. The response profile of DCN neurons is primarily determined by the activity of the PC inputs, their firing rate, and the level of synchrony in their firing [143]. Therefore, the decreased PC activity, as well as the PC degeneration we observed in this study, support the notion that PC properties are exerting a profound influence on the function of DCN output neurons.

In our earlier study measuring excitatory motor neurons and inhibitory ventral horn interneurons (vINs) of SMA mice in the spinal cord [54], we found that MNs displayed a greater excitability, which is supported by other studies [78,145,146]. Similarly, in the cerebellum we observed higher excitability in DCN output neurons from SMA mice in this study. Both MNs and DCN neurons are excitatory neurons, suggesting that disruptions in neuronal excitability may be a common pathology of SMA-affected excitatory neurons. Our study suggests that the disruption of afferent and efferent pathways, selective neurodegeneration, and reactive gliosis may alter the output of the cerebellum and disrupt fine-tuned and precise motor function in SMA patients.

3.6 | Conclusion

This study provides for the first time a detailed characterization of the pathological defects in SMA cerebellum using the SMN Δ 7 mice model and a multi-technique approach. Our findings emphasize that dysfunction in PCs, cerebellar glia, and cerebellar pathways are important facets of SMA disease pathogenesis (Figure S4). Our findings join a growing body of research that supports the notion of SMA as a multi-system disease, with many relevant defects beyond just the lower motor neuron in the spinal cord. By continuing investigation into SMA as a multi-system disease, we can begin to understand whether the pathology observed outside of the spinal cord and in the cerebellum is a result of independent mechanisms due to reduced functional SMN in specific cerebellar cell types, or if it is a downstream effect of neuromuscular and spinal ventral horn degeneration in the spinal cord.

Clinically, SMA pathology in the cerebellum may contribute to the persistent phenotypes that continue to be observed in treated SMA patients. This is especially important considering that the most recently developed treatment for SMA, onasemnogene abeparvovec, has shown relatively little SMN1 delivery to the cerebellum in an infant with SMA type 1 [107]. Optimistically, further investigation into supra-spinal pathology in SMA may reveal novel avenues for therapeutics and treatments in clinical experimentation that could address the persistent deficiencies. While this study provides answers regarding cerebellar defects due to SMA, it also raises many questions about the role that SMN plays across cerebellar cell types and beyond.

4 | MATERIALS AND METHODS

4.1 | Animals

All animal procedures were approved by the Institutional Animal Care and Use Committee of Delaware State University. Mice were maintained under a 14/10 h light/dark photoperiod with PMI rodent diet (Animal Specialties and Provisions) and water available ad libitum. Heterozygote male and female mice of the FVB.Cg-Grm7 < Tg (SMN2)89Ahmb > Snn1 < tm1Msd > Tg (SMN2*delta7) 4299 strain obtained from Jackson Laboratory (stock#: 005025, Bar Harbor, ME) were mated to produce pups for experiments. Post-natal day (P12) pups of both sexes were used for the western blot, MRI, and IHC experiments, and P11-P12 pups were used for the electrophysiology experiments. Mouse genotyping was done by Transnetyx (Germantown, TN) after experimentation and data analyses, but before performing statistical tests for significance. Wild type and heterozygous pups were pooled as controls, and pups with the homozygous mutation formed the SMA group as described previously [41].

4.2 | SMN Western blot analysis and quantification

P12 SMN Δ 7 mice were anesthetized with isoflurane in an upward flowing BSL2 cabinet. After decapitation, brain tissue samples were dissected, submerged in liquid nitrogen for 2 min, then stored at -80°C . The dissected tissues included the cerebellum, brainstem, thalamus, hippocampus, spinal cord, cortex 1, and cortex 2 (cortices were divided coronally within bregma -1 to 0 mm; [147]). For western blotting, tissues were thawed and homogenized on ice by sonification in radioimmunoprecipitation assay buffer (RIPA buffer; ThermoFisher Scientific) with protease inhibitor (Halt Protease Inhibitor Cocktail; ThermoFisher Scientific). Samples were centrifuged for 15 min at 4°C at $15,000g$. Protein lysates were transferred to a new tube and the concentration of the samples was determined using the BCA protein assay kit (ThermoFisher Scientific). Protein concentration was normalized for all samples at $1\ \mu\text{g}/\mu\text{L}$ with an equal volume of 2X SDS sample buffer. The samples were boiled for 5 min and stored at -80°C for later use. Protein samples were loaded onto a 4%–12% Bis-Tris gradient gel (ThermoFisher Scientific), and the gel was run at 50 V for 15 min, followed by 1 h at 140 V. Samples were transferred onto a polyvinylidene difluoride (PVDF) membrane using the Transblot Turbo Transfer System (BioRad). The membranes were blocked for 1 h at room temperature in 5% milk powder in 20 mM Tris pH 7.5, 150 mM NaCl containing 0.1% Tween-20 (TBST). The membranes were then incubated overnight at 4°C in primary antibody solution (mouse anti-SMN, BD Bioscience 61046, 1:1000; anti-beta tubulin, Abcam ab6046, 1:5000).

Antibodies were diluted in 5% milk/TBST buffer described previously. Membranes were washed 3×10 min in 1X TBST at room temperature before 1 h incubation in secondary antibody solution (HRP-conjugated goat anti-mouse; HRP-conjugated goat anti-rabbit, Jackson ImmunoResearch, 1:5000). Secondary antibodies were also diluted in 5% milk/TBST blocking buffer. Membranes were washed 3×10 min in 1X TBST at room temperature and visualized using a chemiluminescent reagent (Pierce™ ECL Western Blotting Substrate) according to the manufacturer's instructions. Membranes were imaged using GeneSys image capture software (Syngene).

Intensity levels of β -tubulin and SMN signals were determined using ImageJ (imagej.nih.gov; [148]) and SMN levels were normalized to β -tubulin signal levels to control for variation in protein loading. The relative decrease of SMN expression in SMA was determined by calculating the average SMN expression found within the cerebellar tissue of three control mice. This value was defined as 1. SMN expression in SMA mice was then obtained by dividing the normalized expression in SMA samples by the average normalized expression in the cerebellar tissue of the controls. With a normalized, relative expression value for each sample, this allows SMN expression to be directly compared across tissues collected from different regions of the brain.

4.3 | MRI scanning and analysis

MRI were obtained using a 9.4 T Bruker Biospec 94/20 small animal MR system (Bruker BioSpec MRI, Ettlingen Germany) in the Center for Biomedical and Brain Imaging at University of Delaware. Mouse brains were extracted at P12, fixed in 4% paraformaldehyde, and stored at 4°C. Control and mutant mouse brains were fixed for at least 2 weeks before being submerged in fomblin oil for ex-vivo MRI. We collected high-quality T2-weighted anatomical imaging sets using the turbo rapid acquisition with relaxation enhancement (turboRARE) pulse sequence, which were performed with the following parameters: a repetition time of 2.5 s, an echo time of 56 ms, 2 averages, isotropic $100 \mu\text{m}^3$ voxel resolution, and a rare factor of 14. The scan time was 1 h 15 min. We acquired diffusion weighted images using a spin-echo echo-planar imaging sequence with the following parameters: an echo time of 45 ms, a repetition time of 500 ms, isotropic $100 \mu\text{m}^3$ voxel resolution, 65 sampling directions with a b -value of 4000 s/mm^2 , 5 $b = 0 \text{ s/mm}^2$ images, a slice thickness a 0.1 mm, fat suppression and field-of-view saturation. The scan time was 2 h 10 min for each brain.

4.4 | MRI volumetric measurements

We acquired volumetric measurements of whole brains and cerebella via segmentation implemented with ITK-SNAP

(itksnap.org). We used T2-weighted images as a guide for brain anatomy, manual segmentation for the cerebella and semi-automatic segmentation was performed for the whole brain. From these segmentations, we generated 3D renditions and volumetric measurements within the program. Regions that were lost during the extraction or scanning process were extrapolated using the Allen Brain Atlas (mouse.brain-map.org). We acquired morphological measurements of the cerebellar width, as well as vermis and hemisphere heights and depths using T2-weighted scans and a ruler tool in DSI-Studio (dsi-studio.labsolver.org). These measurements were used for comparison between control and SMA-affected mice.

4.5 | DTI probabilistic tractography and diffusivity metric analysis

Fiber tract reconstructions were generated from diffusion weighted MR scans via an interpolated streamline propagation algorithm in Diffusion Toolkit (trackvis.org). Tracts were set to cease when the angle between two consecutive orientation vectors (angle threshold) was greater than 45° [149]. An automatic mask threshold with a T2 mask image was found to be most effective in optimizing tract reconstruction and minimizing external tract formation due to background noise. Voxel-based investigation across sagittal sections that span the cerebellum were used to better characterize different tract types. Based on these observations, five tract classifications were generated: IPT, SPT, MPT, ICC, and NTF. IPTs travel through the inferior peduncle and connect to the spinal cord, and are primarily composed of spinocerebellar tracts (SCTs) [150]. SPTs consist of mostly output pathways that travel through the superior peduncle to mainly connect with the midbrain and in few cases the frontal cortex. MPTs pass through the middle peduncle and connect the cerebellum to the cerebral cortex via the pontine nucleus. Categorizing tracts within the cerebellum was impossible with the current resolution, so fibers that did not leave the cerebellum were classified as ICCs. Using these classifications, tract occurrence was quantified on individual sagittal planes for 50 randomly selected single-voxel ROIs [151]. This was done on seven sagittal planes spaced with equal intervals of 500 microns to cover a cerebellar hemisphere and half of the vermis region based on the symmetric pathology of SMA [9] (see Figure 3A–E). Occurrence of each tract type was quantified as a percentage of 50 total voxels. We considered this quantification a reliable strategy to compare cerebellar connectivity to the CNS across disease-affected brains and controls since the tractography identifies large brain pathways and may be less precise at gray to white matter boundaries [152].

Diffusivity metrics of the DTI scans were measured across the entire cerebellum in the mediolateral direction.

We generated single-layer ROIs on sagittal planes at intervals of 200 microns using DSI-Studio. FA, as well as mean, radial, and axial diffusivity (MD, RD, AD, respectively) were obtained as average values from every whole-plane sagittal ROI spanning the cerebellum and tracked for comparison between disease-affected cerebella and controls. Midpoint values were aligned across brains for anatomical consistency during statistical analysis.

4.6 | Immunohistochemistry, imaging, and analysis

IHC staining with low and high magnification imaging were performed at the Histochemistry and Tissue Processing Core Laboratory at Nemours A.I. duPont Children's Hospital in Wilmington, Delaware. SMA-affected ($n = 6$) and control brains ($n = 6$) were bisected along the sagittal plane and processed for 1 h on an ASP300S tissue processor (Leica, Buffalo Grove, IL). Four out of six brains for both SMA-affected and control that were used for IHC and had also been used for MRI scanning. We chose this approach to enhance comparative power across structural information and cellular function. Each brain was bisected along the sagittal plane and paraffin-embedded on a single block; one half was embedded with the medial side down, while the other half was embedded with the lateral side down. Then for each brain, two slices of $5\ \mu\text{m}$ were floated onto one Superfrost Plus slide (Fisher Scientific, Pittsburg, PA). This was done three times with each pair of sections on an individual slide; each slide was stained with one of the following antibodies: anti-calbindin antibody (Abcam ab229915) for PC staining, Anti-GFAP antibody (Abcam ab207165) for astrocyte staining, and Anti-NeuN antibody (Abcam ab177487) for granule cell staining. For each brain, this was done twice in two regions within the intermediate zone of the cerebellum. Slides were incubated for 30 min in one of the three antibodies, incubated in a Peroxide Block, developed in DAB and counter-stained with hematoxylin to visualize the nucleus of the cells. The slides were dried with ethanol, then xylene, and cover-slipped with Tissue-Tek[®] Prisma[™] mounting media (Sakura, Torrance, CA). Imaging of the cerebellar slices was performed with an Olympus Bx51 Microscope (Olympus, Waltham, MA) for all three stains. The three antibodies combined with hematoxylin counterstaining enabled morphological analyses. All immunoreactive analyses were performed using QuPath (qupath.github.io) brightfield H-DAB cell detection function with parameters of $\sigma = 8\ \text{px}$, $\text{threshold} = 0.1$, $\text{cell expansion} = 1\ \text{px}$.

PC count per slice and PC soma size were acquired via cell detection using the $4\times$ images of calbindin staining. Using QuPath, single-lobule ROIs were acquired in accordance with the Allen Brain Atlas

(<http://atlas.brain-map.org>). From these ROIs, area and perimeter measurements were generated. PCs were manually counted within each of the lobules (CUL 4/5, SIM, ANCr1, ANCr2, PRM, COPY), and area and perimeter densities were calculated. Granule cells could not be differentiated in the internal and external granule layers (IGL and EGL, respectively) during cell detection via NeuN staining due to the small and compact organization of the granule cells in young mice. Thus, thickness measurements of the IGL, PC, and MLs (PCL and ML), and EGL were acquired to assess cerebellar abnormalities in morphology and GCP. Three technical replicates were acquired for each layer from the lobes that were least and most affected based on the PC defects. This was done for the six biological replicates in both the SMA and control groups using the ruler tool in QuPath.

A BioTek Cytation 5 imaging reader (Winooski, VT, USA) was used for $20\times$ imaging of NeuN stains in the ML of the cerebellum to quantify the migrating granule cells. Based on the lobule and PC defects, the least and most affected lobules were imaged. This provides comparative power between corresponding SMA and CTL lobes as well as between lobes within SMA cerebella. Granule cells were detected and quantified in the ML for each lobe and cell density measurements were calculated (number of detections/ mm^2). NeuN staining was also present in DCN neurons. Neuronal somas were detected in the DCN with the $4\times$ images; cell density was calculated in μm^2 and soma areas were acquired in μm^2 for comparison.

The $4\times$ GFAP images were used to assess the robustness and integrity of glial cells across the cerebellar white and gray matter. Unfortunately, we were unable to assess individual glial cell size and morphology due to the clustered and layered nature of this cell type, as well as imaging resolution. However, for the white matter regions of the cerebellum including the branched arbor vitae and peduncles, ROIs were hand drawn using an Allen Brain Atlas for reference (see Figure 6A,B), and measurements were acquired in units of optical density and positive pixels per μm^2 , and were converted to mm^2 where appropriate. Lobule-specific values were acquired where appropriate. The same was performed for the gray matter regions of the cerebellum, such as the ML, IGL, and DCN (see Figure 7A,B).

4.7 | Acute cerebellum slice preparation

P11-12 mice were anesthetized in a sealed chamber containing the inhalation anesthetic isoflurane in an upward flowing BSL2 cabinet. After decapitation, the brain was quickly removed and immersed in the ice-cold oxygenated slicing solution contained: 2.5 mM KCl, 10 mM MgSO_4 , 0.5 mM CaCl_2 , 1.25 mM NaH_2PO_4 , 234 mM sucrose, 11 mM glucose, and 26 mM NaHCO_3 (pH 7.2, 310–330 mOsm). The 300- μm sagittal slices were cut with

a LEICA VT1200s tissue slicer (Leica Microsystems, Wentzler, Germany) in ice-cold oxygenated slicing solution. Slices were incubated in oxygenated slicing solution at 34°C for 30 min, then left at room temperature for more than 60 min before electrophysiology recordings.

4.8 | Electrophysiological recordings and analysis

After at least 1 h of recovery, the slices were transferred to a recording chamber, which was continuously perfused at a rate of 2–3 mL/min with pre-heated 34°C artificial cerebrospinal fluid containing: 126 mM NaCl, 3 mM KCl, 2 mM MgCl₂, 2 mM CaCl₂, 1.25 mM NaH₂PO₄, 10 mM glucose, and 26 mM NaHCO₃ (pH 7.2, 310–330 mOsm). The DCN glutamatergic output neurons were selected for our study by their morphology and physiological signatures: largest soma (>20 μm), complex dendrites, high frequency of spontaneous firing and short rebound depolarization associated firing [53]. Alexa 594 (50 μM) was included in the intracellular solution to show the morphology of the neuron immediately after recording. The internal solution contained (in mM): 130 K-gluconate, 10 Hepes, 11 EGTA, 2.0 MgCl₂, 2.0 CaCl₂, 4 5'-ATP-Na₂, and 0.2 5'-GTP-Na₂ (pH 7.2–7.3, 290–310 mOsm). Only neurons with greater than 20 μm soma diameter, complex dendritic branches, spontaneous firing, and less than 500 ms rebound depolarization, which are the signature characteristics of glutamatergic output neurons, were included in the analysis. The cell-attached mode was first employed to record spontaneous firing of the neuron under voltage-clamp mode to avoid any effect of the internal solution. Then whole-cell configuration was employed afterwards by breaking through the membrane with negative pressure. Current-clamp recordings were acquired via Clampex 11 by a Multi-Clamp 700B amplifier with auto bridge balance. Data were filtered with low pass at 10 KHz and digitized at 100 kHz with a Digidata 1550B (Molecular Devices; Sunnyvale, CA). The membrane potential was held at –60 mV by manual current injection for all current-clamp recordings. Single action potentials were evoked every 5 s with positive current injection steps of 50 pA intervals. The input resistance, time constant, and firing frequency versus injection current (F-I) relationship was studied by 1 s negative and positive steps with 20 pA intervals applied every 10 s.

Data were analyzed with Clampfit 11 (Molecular Devices; Sunnyvale, CA). Membrane input resistance (Rin) was calculated from the mean voltage deflections during the last 50 ms of the 1 s hyperpolarizing current pulse injection. The membrane time constant (Tau) was derived from an exponential decay fit applied to the beginning 100 ms of the current-evoked membrane hyperpolarization. The capacitance of the membrane (Cm) was calculated by the measurement of Rin and Tau

(Cm = Tau/Rin). Action potential (AP) peak amplitude was measured from the first AP evoked. AP threshold was defined as the membrane potential at which dV/dt first exceeds 10 V/s [153]. The minimum current required to evoke the first AP was defined as the rheobase current. The firing frequency for F-I relationship was measured by the mean frequency of each current injection step. The baseline for determining the ADP and the AHP was the membrane potential before AP activation (–60 mV). For details of the electrophysiology recordings and analysis, please refer to previous publications [41,54].

4.9 | Statistical analysis

All statistical analysis was carried out in the Graphpad Prism 9 software (graphpad.com). For western blot analysis, we used unpaired two-tailed Student's *t*-tests to determine significance across SMA and control groups. Between the cerebellum and brain regions within control brains and SMA brains, we used an ordinary one-way ANOVA with Šidák's multiple comparisons test since comparisons were made between preselected pairs of columns. In the morphometric analysis, unpaired two-tailed Student's *t*-tests were used to compare volumes and volume ratios. For the tractography and diffusivity metric analyses, multiple unpaired two-tailed Student's *t*-tests were used. For histological analyses, unpaired two-tailed Student's *t*-tests were used, as well as ordinary one-way ANOVAs with Tukey's multiple comparisons test where appropriate since each column was compared with the mean of every other column. For the electrophysiological measurements, unpaired one-tailed Student's *t*-tests were used to compare frequencies and gain. Multiple unpaired Student's *t*-tests with Welch correction were used for the frequency comparisons at each current injection value. P values are indicated as follows: *, $p < 0.05$; **, $p < 0.01$; ***, $p < 0.001$; °, $0.5 < p < 0.10$. Figure legends indicate where # or • are used for other statistical comparisons. All quantification data are plotted as means ± standard errors of the means (SEM).

AUTHOR CONTRIBUTIONS

Nicholas C. Cottam: Conceptualization; methodology; formal analysis; investigation; resources; data curation; writing—original draft and preparation; and visualization. **Tiffany Bamfo:** Investigation; visualization. **Melissa Harrington:** Conceptualization; methodology; writing—review and editing; supervision; funding acquisition. **Christine Charvet:** Methodology; writing—review and editing; visualization. **Khan Hekmatyar:** Methodology; software; investigation. **Nikita Tulin:** Data curation. **Jianli Sun:** Conceptualization; methodology; formal analysis; investigation; writing—review and editing; visualization; supervision; project administration; funding acquisition.

ACKNOWLEDGMENTS

We would like to acknowledge Dr. Julian Woollorton for his intellectual contribution, Dr. Fang-Cheng Yeh for his help using the DSI Studio software (dsi-studio.labsolver.org), Dr. Hakeem Lawal for his help in creating the summary figure, and Khaliyah White for her help on western blotting experiments.

CONFLICT OF INTEREST STATEMENT

The authors declare no conflicts of interest.

DATA AVAILABILITY STATEMENT

We acquired no data from publicly available sources.

ORCID

Nicholas C. Cottam  <https://orcid.org/0000-0001-6300-8999>

Melissa A. Harrington  <https://orcid.org/0000-0002-6159-4477>

Christine J. Charvet  <https://orcid.org/0000-0002-0985-3056>

Jianli Sun  <https://orcid.org/0000-0003-0159-689X>

REFERENCES

- Sugarman EA, Nagan N, Zhu H, Akmaev VR, Zhou Z, Rohlf's EM, et al. Pan-ethnic carrier screening and prenatal diagnosis for spinal muscular atrophy: clinical laboratory analysis of >72,400 specimens. *Eur J Hum Genet.* 2012;20:27–32.
- Verhaart IEC, Robertson A, Wilson IJ, Aartsma-Rus A, Cameron S, Jones CC, et al. Prevalence, incidence and carrier frequency of 5q-linked spinal muscular atrophy – a literature review. *Orphanet J Rare Dis.* 2017;12:124.
- Lefebvre S, Bürglen L, Reboullet S, Clermont O, Burlet P, Viollet L, et al. Identification and characterization of a spinal muscular atrophy-determining gene. *Cell.* 1995;80:155–65.
- Lunn MR, Wang CH. Spinal muscular atrophy. *Lancet.* 2008;371:2120–33.
- Stam M, Haakma W, Kuster L, Froeling M, Philippens MEP, Bos C, et al. Magnetic resonance imaging of the cervical spinal cord in spinal muscular atrophy. *Neuroimage Clin.* 2019;24:102002.
- Calucho M, Bernal S, Alías L, March F, Venceslá A, Rodríguez-Álvarez FJ, et al. Correlation between SMA type and SMN2 copy number revisited: an analysis of 625 unrelated Spanish patients and a compilation of 2834 reported cases. *Neuromuscul Disord.* 2018;28:208–15.
- Chaytow H, Huang YT, Gillingwater TH, Faller KME. The role of survival motor neuron protein (SMN) in protein homeostasis. *Cell Mol Life Sci.* 2018;75:3877–94.
- Farrar MA, Kiernan MC. The genetics of spinal muscular atrophy: progress and challenges. *Neurotherapeutics.* 2015;12:290–302.
- Kolb SJ, Kissel JT. Spinal muscular atrophy. *Neurol Clin.* 2015;33:831–46.
- Vitte J, Fassier C, Tiziano FD, Dalard C, Soave S, Roblot N, et al. Refined characterization of the expression and stability of the SMN gene products. *Am J Pathol.* 2007;171:1269–80.
- Burghes AH, Beattie CE. Spinal muscular atrophy: why do low levels of survival motor neuron protein make motor neurons sick? *Nat Rev Neurosci.* 2009;10:597–609.
- Pellizzoni L, Yong J, Dreyfuss G. Essential role for the SMN complex in the specificity of snRNP assembly. *Science.* 2002;298:1775–9.
- Wan L, Battle DJ, Yong J, Gubitz AK, Kolb SJ, Wang J, et al. The survival of motor neurons protein determines the capacity for snRNP assembly: biochemical deficiency in spinal muscular atrophy. *Mol Cell Biol.* 2005;25:5543–51.
- Zhang Z, Lotti F, Dittmar K, Younis I, Wan L, Kasim M, et al. SMN deficiency causes tissue-specific perturbations in the repertoire of snRNAs and widespread defects in splicing. *Cell.* 2008;133:585–600.
- Ruggiu M, McGovern VL, Lotti F, Saieva L, Li DK, Kariya S, et al. A role for SMN exon 7 splicing in the selective vulnerability of motor neurons in spinal muscular atrophy. *Mol Cell Biol.* 2012;32:126–38.
- Hamilton G, Gillingwater TH. Spinal muscular atrophy: going beyond the motor neuron. *Trends Mol Med.* 2013;19:40–50.
- Masson R, Brusa C, Scoto M, Baranello G. Brain, cognition, and language development in spinal muscular atrophy type 1: a scoping review. *Dev Med Child Neurol.* 2021;63:527–36.
- Nash LA, Burns JK, Chardon JW, Kothary R, Parks RJ. Spinal muscular atrophy: more than a disease of motor neurons? *Curr Mol Med.* 2016;16:779–92.
- Yeo CJJ, Darras BT. Overturning the paradigm of spinal muscular atrophy as just a motor neuron disease. *Pediatr Neurol.* 2020;109:12–9.
- Reilly A, Deguise M-O, Beauvais A, Yaworski R, Thebault S, Tessier DR, et al. Central and peripheral delivery of AAV9-SMN target different pathomechanisms in a mouse model of spinal muscular atrophy. *Gene Ther.* 2022;29(9):544–554.
- Araki S, Hayashi M, Tamagawa K, Saito M, Kato S, Komori T, et al. Neuropathological analysis in spinal muscular atrophy type II. *Acta Neuropathol.* 2003;106:441–8.
- Bebee TW, Dominguez CE, Chandler DS. Mouse models of SMA: tools for disease characterization and therapeutic development. *Hum Genet.* 2012;131:1277–93.
- Harding BN, Kariya S, Monani UR, Chung WK, Benton M, Yum SW, et al. Spectrum of neuropathophysiology in spinal muscular atrophy type I. *J Neuropathol Exp Neurol.* 2015;74:15–24.
- Querin G, El Mendili M-M, Lenglet T, Behin A, Stojkovic T, Salachas F, et al. The spinal and cerebral profile of adult spinal-muscular atrophy: a multimodal imaging study. *Neuroimage Clin.* 2019;21:101618.
- Martinez TL, Kong L, Wang X, Osborne MA, Crowder ME, Van Meerbeke JP, et al. Survival motor neuron protein in motor neurons determines synaptic integrity in spinal muscular atrophy. *J Neurosci.* 2012;32:8703–15.
- Monani UR. Spinal muscular atrophy: a deficiency in a ubiquitous protein; a motor neuron-specific disease. *Neuron.* 2005;48:885–96.
- Devriendt K, Lammens M, Schollen E, Van Hole C, Dom R, Devlieger H, et al. Clinical and molecular genetic features of congenital spinal muscular atrophy. *Ann Neurol.* 1996;40:731–8.
- Ito Y, Kumada S, Uchiyama A, Saito K, Osawa M, Yagishita A, et al. Thalamic lesions in a long-surviving child with spinal muscular atrophy type I: MRI and EEG findings. *Brain Dev.* 2004;26:53–6.
- Towfighi J, Young RS, Ward RM. Is Werdnig-Hoffmann disease a pure lower motor neuron disorder? *Acta Neuropathol.* 1985;65:270–80.
- Liu H, Shafey D, Moores JN, Kothary R. Neurodevelopmental consequences of Smn depletion in a mouse model of spinal muscular atrophy. *J Neurosci Res.* 2010;88:111–22.
- Battaglia G, Princivalle A, Forti F, Lizier C, Zeviani M. Expression of the SMN gene, the spinal muscular atrophy determining gene, in the mammalian central nervous system. *Hum Mol Genet.* 1997;6:1961–71.
- Wishart TM, Huang JP-W, Murray LM, Lamont DJ, Mutsaers CA, Ross J, et al. SMN deficiency disrupts brain development in a mouse model of severe spinal muscular atrophy. *Hum Mol Genet.* 2010;19:4216–28.

33. Mendonça RH, Rocha AJ, Lozano-Arango A, Diaz AB, Castiglioni C, Silva AMS, et al. Severe brain involvement in 5q spinal muscular atrophy type 0. *Ann Neurol*. 2019;86:458–62.
34. Maeda K, Chong PF, Yamashita F, Akamine S, Kawakami S, Saito K, et al. Global central nervous system atrophy in spinal muscular atrophy type 0. *Ann Neurol*. 2019;86:801–2.
35. d'Errico P, Boido M, Piras A, Valsecchi V, De Amicis E, Locatelli D, et al. Selective vulnerability of spinal and cortical motor neuron subpopulations in delta7 SMA mice. *PLOS One*. 2013;8:e82654.
36. Manto M, Bower JM, Conforto AB, Delgado-García JM, da Guarda SNF, Gerwig M, et al. Consensus paper: roles of the cerebellum in motor control—the diversity of ideas on cerebellar involvement in movement. *Cerebellum*. 2012;11:457–87.
37. Huang C-m, Wang L, Huang RH. Cerebellar granule cell: ascending axon and parallel fiber. *Eur J Neurosci*. 2006;23:1731–7.
38. Giavazzi A, Setola V, Simonati A, Battaglia G. Neuronal-specific roles of the survival motor neuron protein: evidence from survival motor neuron expression patterns in the developing human central nervous system. *J Neuropathol Exp Neurol*. 2006;65:267–77.
39. Tizzano EF, Cabot C, Baiget M. Cell-specific survival motor neuron gene expression during human development of the central nervous system: implications for the pathogenesis of spinal muscular atrophy. *Am J Pathol*. 1998;153:355–61.
40. de Borba FC, Querin G, França MC, Pradat PF. Cerebellar degeneration in adult spinal muscular atrophy patients. *J Neurol*. 2020;267:2625–31.
41. Tharaneetharan A, Cole M, Norman B, Romero NC, Woollorton JRA, Harrington MA, et al. Functional abnormalities of cerebellum and motor cortex in spinal muscular atrophy mice. *Neuroscience*. 2021;452:78–97.
42. Kanamaru Y, Li J, Stewart N, Sidman RL, Takahashi E. Cerebellar pathways in mouse model of Purkinje cell degeneration detected by high-angular resolution diffusion imaging Tractography. *Cerebellum*. 2017;16:648–55.
43. Charvet CJ, Ofori K, Baucum C, Sun J, Modrell MS, Hekmatyar K, et al. Tracing modification to cortical circuits in human and nonhuman primates from high-resolution tractography, transcription, and temporal dimensions. *J Neurosci*. 2022;42:3749–67.
44. Chu Z, Wilde EA, Hunter JV, McCauley SR, Bigler ED, Troyanskaya M, et al. Voxel-based analysis of diffusion tensor imaging in mild traumatic brain injury in adolescents. *Am J Neuroradiol*. 2010;31:340–6.
45. Loane DJ, Byrnes KR. Role of microglia in neurotrauma. *Neurotherapeutics*. 2010;7:366–77.
46. Chang EH, Argyelan M, Aggarwal M, Chandon TS, Karlsgodt KH, Mori S, et al. The role of myelination in measures of white matter integrity: combination of diffusion tensor imaging and two-photon microscopy of CLARITY intact brains. *Neuroimage*. 2017;147:253–61.
47. Alexander AL, Hurley SA, Samsonov AA, Adluru N, Hosseinbor AP, Mossahebi P, et al. Characterization of cerebral white matter properties using quantitative magnetic resonance imaging stains. *Brain Connect*. 2011;1:423–46.
48. Whitney ER, Kemper TL, Rosene DL, Bauman ML, Blatt GJ. Calbindin-D28k is a more reliable marker of human Purkinje cells than standard Nissl stains: a stereological experiment. *J Neurosci Methods*. 2008;168:42–7.
49. Guseĭnikova VV, Korzhhevskiy DE. NeuN As a neuronal nuclear antigen and neuron differentiation marker. *Acta Naturae*. 2015;7:42–7.
50. Hanzel M, Rook V, Wingate RJT. Mitotic granule cell precursors undergo highly dynamic morphological transitions throughout the external germinal layer of the chick cerebellum. *Sci Rep*. 2019;9:15218.
51. Abati E, Citterio G, Bresolin N, Comi GP, Corti S. Glial cells involvement in spinal muscular atrophy: could SMA be a neuroinflammatory disease? *Neurobiol Dis*. 2020;140:104870.
52. Freigang M, Steinacker P, Wurster CD, Schreiber-Katz O, Osmanovic A, Petri S, et al. Glial fibrillary acidic protein in cerebrospinal fluid of patients with spinal muscular atrophy. *Ann Clin Transl Neurol*. 2022;9:1437–48.
53. Uusisaari M, Knöpfel T. Functional classification of neurons in the mouse lateral cerebellar nuclei. *Cerebellum*. 2011;10:637–46.
54. Sun J, Harrington MA. The alteration of intrinsic excitability and synaptic transmission in lumbar spinal motor neurons and interneurons of severe spinal muscular atrophy mice. *Front Cell Neurosci*. 2019;13:15.
55. Le TT, Pham LT, Butchbach MER, Zhang HL, Monani UR, Coover DD, et al. SMNΔ7, the major product of the centromeric survival motor neuron (SMN2) gene, extends survival in mice with spinal muscular atrophy and associates with full-length SMN. *Hum Mol Genet*. 2005;14:845–57.
56. Arnold WD, Porensky PN, McGovern VL, Iyer CC, Duque S, Li X, et al. Electrophysiological biomarkers in spinal muscular atrophy: preclinical proof of concept. *Ann Clin Transl Neurol*. 2014;1:34–44.
57. Arnold WD, Duque S, Iyer CC, Zaworski P, McGovern VL, Taylor SJ, et al. Normalization of patient-identified plasma biomarkers in SMNΔ7 mice following postnatal SMN restoration. *PLoS One*. 2016;11:e0167077.
58. Swoboda KJ, Prior TW, Scott CB, McNaught TP, Wride MC, Reyna SP, et al. Natural history of denervation in SMA: relation to age, SMN2 copy number, and function. *Ann Neurol*. 2005;57:704–12.
59. Weng WC, Hsu YK, Chang FM, Lin CY, Hwu WL, Lee WT, et al. CMAP changes upon symptom onset and during treatment in spinal muscular atrophy patients: lessons learned from newborn screening. *Genet Med*. 2021;23:415–20.
60. Palermo L, Di Vita A, Boccia M, Nemmi F, Brunelli S, Traballese M, et al. Action and non-action oriented body representations: insight from behavioural and grey matter modifications in individuals with lower limb amputation. *Biomed Res Int*. 2018;2018:1529730–11.
61. Jacobi H, Reetz K, du Montcel ST, Bauer P, Mariotti C, Nanetti L, et al. Biological and clinical characteristics of individuals at risk for spinocerebellar ataxia types 1, 2, 3, and 6 in the longitudinal RISCA study: analysis of baseline data. *Lancet Neurol*. 2013;12:650–8.
62. Reetz K, Rodríguez-Labrada R, Dogan I, Mirzazade S, Romanzetti S, Schulz JB, et al. Brain atrophy measures in preclinical and manifest spinocerebellar ataxia type 2. *Ann Clin Transl Neurol*. 2018;5:128–37.
63. Rezende TJR, de Paiva JLR, Martinez ARM, Lopes-Cendes I, Pedroso JL, Barsottini OGP, et al. Structural signature of SCA3: from presymptomatic to late disease stages. *Ann Neurol*. 2018;84:401–8.
64. Velázquez-Pérez L, Rodríguez-Labrada R, Cruz-Rivas EM, Fernández-Ruiz J, Vaca-Palomares I, Lilia-Campins J, et al. Comprehensive study of early features in spinocerebellar ataxia 2: delineating the prodromal stage of the disease. *Cerebellum*. 2014;13:568–79.
65. Ventura-Antunes L, Mota B, Herculano-Houzel S. Different scaling of white matter volume, cortical connectivity, and gyrification across rodent and primate brains. *Front Neuroanat*. 2013;7:15253–61.
66. Sudarov A, Joyner AL. Cerebellum morphogenesis: the foliation pattern is orchestrated by multi-cellular anchoring centers. *Neural Dev*. 2007;2:26.
67. Goveas J, O'Dwyer L, Mascalchi M, Cosottini M, Diciotti S, De Santis S, et al. Diffusion-MRI in neurodegenerative disorders. *Magn Reson Imaging*. 2015;33:853–76.
68. Nölle A, Zeug A, van Bergeijk J, Tönges L, Gerhard R, Brinkmann H, et al. The spinal muscular atrophy disease protein

- SMN is linked to the Rho-kinase pathway via profilin. *Hum Mol Genet.* 2011;20:4865–78.
69. Rossoll W, Jablonka S, Andreassi C, Kröning AK, Karle K, Monani UR, et al. Smn, the spinal muscular atrophy-determining gene product, modulates axon growth and localization of beta-actin mRNA in growth cones of motoneurons. *J Cell Biol.* 2003;163:801–12.
 70. Saal L, Briese M, Kneitz S, Glinka M, Sendtner M. Subcellular transcriptome alterations in a cell culture model of spinal muscular atrophy point to widespread defects in axonal growth and presynaptic differentiation. *RNA.* 2014;20:1789–802.
 71. Setola V, Terao M, Locatelli D, Bassanini S, Garattini E, Battaglia G. Axonal-SMN (a-SMN), a protein isoform of the survival motor neuron gene, is specifically involved in axonogenesis. *Proc Natl Acad Sci.* 2007;104:1959–64.
 72. van Bergeijk J, Rydel-Könecke K, Grothe C, Claus P. The spinal muscular atrophy gene product regulates neurite outgrowth: importance of the C terminus. *FASEB J.* 2007;21:1492–502.
 73. Koh M, Markovich B. *Neuroanatomy, spinocerebellar dorsal tract.* StatPearls. Tampa: StatPearls Publishing LLC; 2022.
 74. Duman O, Uysal H, Skjei KL, Kizilay F, Karauzum S, Haspolat S. Sensorimotor polyneuropathy in patients with SMA type-1: electroneuromyographic findings. *Muscle Nerve.* 2013;48:117–21.
 75. Rudnik-Schöneborn S, Goebel HH, Schlote W, Molaian S, Omran H, Ketelsen U, et al. Classical infantile spinal muscular atrophy with SMN deficiency causes sensory neuropathy. *Neurology.* 2003;60:983–7.
 76. Jablonka S, Karle K, Sandner B, Andreassi C, von Au K, Sendtner M. Distinct and overlapping alterations in motor and sensory neurons in a mouse model of spinal muscular atrophy. *Hum Mol Genet.* 2006;15:511–8.
 77. Shorrock HK, van der Hoorn D, Boyd PJ, Llaverro Hurtado M, Lamont DJ, Wirth B, et al. UBA1/GARS-dependent pathways drive sensory-motor connectivity defects in spinal muscular atrophy. *Brain.* 2018;141:2878–94.
 78. Mentis GZ, Blivis D, Liu W, Drobac E, Crowder ME, Kong L, et al. Early functional impairment of sensory-motor connectivity in a mouse model of spinal muscular atrophy. *Neuron.* 2011;69:453–67.
 79. Ling KKY, Lin M-Y, Zingg B, Feng Z, Ko C-P. Synaptic defects in the spinal and neuromuscular circuitry in a mouse model of spinal muscular atrophy. *PLoS One.* 2010;5:e15457.
 80. Leergaard TB, Lyngstad KA, Thompson JH, Taeymans S, Vos BP, De Schutter E, et al. Rat somatosensory cerebropontocerebellar pathways: spatial relationships of the somatotopic map of the primary somatosensory cortex are preserved in a three-dimensional clustered pontine map. *J Comp Neurol.* 2000;422:246–66.
 81. Biswas MS, Luo Y, Sarpong G, Sugihara I. Divergent projections of single pontocerebellar axons to multiple cerebellar lobules in the mouse. *J Comp Neurol.* 2019;527:1966–85.
 82. Leergaard TB, Bjaalie J. Topography of the complete corticopontine projection: from experiments to principal maps. *Front Neurosci.* 2007;1:211–23.
 83. Kelly RM, Strick PL. Cerebellar loops with motor cortex and prefrontal cortex of a nonhuman primate. *J Neurosci.* 2003;23:8432–44.
 84. Schmähmann JD, Pandya DN. Prefrontal cortex projections to the basilar pons in rhesus monkey: implications for the cerebellar contribution to higher function. *Neurosci Lett.* 1995;199:175–8.
 85. Grefkes C, Ritzl A, Zilles K, Fink GR. Human medial intraparietal cortex subserves visuomotor coordinate transformation. *Neuroimage.* 2004;23:1494–506.
 86. Pochon JB, Levy R, Poline JB, Crozier S, Lehericy S, Pillon B, et al. The role of dorsolateral prefrontal cortex in the preparation of forthcoming actions: an fMRI study. *Cereb Cortex.* 2001;11:260–6.
 87. Ramnani N, Behrens TE, Johansen-Berg H, Richter MC, Pinsk MA, Andersson JL, et al. The evolution of prefrontal inputs to the cortico-pontine system: diffusion imaging evidence from Macaque monkeys and humans. *Cereb Cortex.* 2006;16:811–8.
 88. Stoodley CJ, Schmähmann JD. Functional topography in the human cerebellum: a meta-analysis of neuroimaging studies. *Neuroimage.* 2009;44:489–501.
 89. Dobromyslin VI, Salat DH, Fortier CB, Leritz EC, Beckmann CF, Milberg WP, et al. Distinct functional networks within the cerebellum and their relation to cortical systems assessed with independent component analysis. *Neuroimage.* 2012;60:2073–85.
 90. He Y, Zang Y, Jiang T, Liang M, Gong G. Detecting functional connectivity of the cerebellum using low frequency fluctuations (LFFs). *Medical Image Computing and Computer-Assisted Intervention – MICCAI.* 907–15. 2004.
 91. Krienen FM, Buckner RL. Segregated fronto-cerebellar circuits revealed by intrinsic functional connectivity. *Cereb Cortex.* 2009;19:2485–97.
 92. Sokolov A, Erb M, Gharabaghi A, Grodd W, Tatagiba M, Pavlova M. Biological motion processing: the left cerebellum communicates with the right superior temporal sulcus. *Neuroimage.* 2012a;59:2824–30.
 93. Sokolov AA, Erb M, Grodd W, Pavlova MA. Structural loop between the cerebellum and the superior temporal sulcus: evidence from diffusion tensor imaging. *Cereb Cortex.* 2012b;24:626–32.
 94. Booth JR, Wood L, Lu D, Houk JC, Bitan T. The role of the basal ganglia and cerebellum in language processing. *Brain Res.* 2007;1133:136–44.
 95. Palesi F, De Rinaldis A, Castellazzi G, Calamante F, Muhlert N, Chard D, et al. Contralateral cortico-ponto-cerebellar pathways reconstruction in humans in vivo: implications for reciprocal cerebro-cerebellar structural connectivity in motor and non-motor areas. *Sci Rep.* 2017;7:12841.
 96. Kamali A, Kramer LA, Frye RE, Butler IJ, Hasan KM. Diffusion tensor tractography of the human brain cortico-ponto-cerebellar pathways: a quantitative preliminary study. *J Magn Reson Imaging.* 2010;32:809–17.
 97. Alexander AL, Lee JE, Lazar M, Field AS. Diffusion tensor imaging of the brain. *Neurotherapeutics.* 2007;4:316–29.
 98. Winkiewicz PJ, Sabisz A, Naumczyk P, Jodzio K, Szurawska E, Szarmach A. Understanding the physiopathology behind axial and radial diffusivity changes—what do we know? *Front Neurol.* 2018;9:92.
 99. Budde MD, Janes L, Gold E, Turtzo LC, Frank JA. The contribution of gliosis to diffusion tensor anisotropy and tractography following traumatic brain injury: validation in the rat using Fourier analysis of stained tissue sections. *Brain.* 2011;134:2248–60.
 100. Reischauer C, Gutzeit A, Neuwirth C, Fuchs A, Sartoretto-Schefer S, Weber M, et al. In-vivo evaluation of neuronal and glial changes in amyotrophic lateral sclerosis with diffusion tensor spectroscopy. *Neuroimage Clin.* 2018;20:993–1000.
 101. Soni N, Medeiros R, Alateeq K, To XV, Nasrallah FA. Diffusion tensor imaging detects acute pathology-specific changes in the P301L tauopathy mouse model following traumatic brain injury. *Front Neurosci.* 2021;15:611451.
 102. Cook AA, Fields E, Watt AJ. Losing the beat: contribution of Purkinje cell firing dysfunction to disease, and its reversal. *Neuroscience.* 2021;462:247–61.
 103. Kuru S, Sakai M, Konagaya M, Yoshida M, Hashizume Y, Saito K. An autopsy case of spinal muscular atrophy type III (Kugelberg-Welander disease). *Neuropathology.* 2009;29:63–7.
 104. Schmitt HP, Härle M, Koelfen W, Nissen KH. Childhood progressive spinal muscular atrophy with facioscapulo-humeral predominance, sensory and autonomic involvement and optic atrophy. *Brain Dev.* 1994;16:386–92.
 105. Serra-Ortega A, Torres A, Segreo M. Spinal muscular atrophy associated with olivopontocerebellar hypoplasia. A case report. *Rev Neurol.* 2005;40:90–2.

106. Jodelka FM, Ebert AD, Duelli DM, Hastings ML. A feedback loop regulates splicing of the spinal muscular atrophy-modifying gene, SMN2. *Hum Mol Genet.* 2010;19:4906–17.
107. Thomsen G, Burghes AHM, Hsieh C, Do J, Chu BTT, Perry S, et al. Biodistribution of onasemnogene abeparvovec DNA, mRNA and SMN protein in human tissue. *Nat Med.* 2021;27:1701–11.
108. Shin SW, Lee MY, Kwon GY, Park JW, Yoo M, Kim SK, et al. Cloning and characterization of rat neuronal apoptosis inhibitory protein cDNA. *Neurochem Int.* 2003;42:481–91.
109. Xu DG, Korneluk RG, Tamai K, Wigle N, Hakim A, Mackenzie A, et al. Distribution of neuronal apoptosis inhibitory protein-like immunoreactivity in the rat central nervous system. *J Comp Neurol.* 1997;382:247–59.
110. Jung BC, Choi SI, Du AX, Cuzzocreo JL, Ying HS, Landman BA, et al. MRI shows a region-specific pattern of atrophy in spinocerebellar ataxia type 2. *Cerebellum.* 2012;11:272–9.
111. El-Khodori BF, Edgar N, Chen A, Winberg ML, Joyce C, Brunner D, et al. Identification of a battery of tests for drug candidate evaluation in the SMN Δ 7 neonate model of spinal muscular atrophy. *Exp Neurol.* 2008;212(1):29–43.
112. Jankowski J, Miething A, Schilling K, Baader SL. Physiological Purkinje cell death is spatiotemporally organized in the developing mouse cerebellum. *Cerebellum.* 2009;8:277–90.
113. Anderton RS, Meloni BP, Mastaglia FL, Boulous S. Spinal muscular atrophy and the antiapoptotic role of survival of motor neuron (SMN) protein. *Mol Neurobiol.* 2013;47:821–32.
114. Liu Q, Dreyfuss G. A novel nuclear structure containing the survival of motor neurons protein. *EMBO J.* 1996;15:3555–65.
115. Iwahashi H, Eguchi Y, Yasuhara N, Hanafusa T, Matsuzawa Y, Tsujimoto Y. Synergistic anti-apoptotic activity between Bcl-2 and SMN implicated in spinal muscular atrophy. *Nature.* 1997;390:413–7.
116. Anderton RS, Price LL, Turner BJ, Meloni BP, Mitrpant C, Mastaglia FL, et al. Co-regulation of survival of motor neuron and Bcl-xL expression: implications for neuroprotection in spinal muscular atrophy. *Neuroscience.* 2012;220:228–36.
117. Frankowski H, Missotten M, Fernandez PA, Martinou I, Michel P, Sadoul R, et al. Function and expression of the Bcl-x gene in the developing and adult nervous system. *Neuroreport.* 1995;6:1917–21.
118. Soler-Botija C, Ferrer I, Alvarez JL, Baiget M, Tizzano EF. Downregulation of Bcl-2 proteins in type I spinal muscular atrophy motor neurons during fetal development. *J Neuropathol Exp Neurol.* 2003;62:420–6.
119. Tsai LK, Tsai MS, Ting CH, Wang SH, Li H. Restoring Bcl-x (L) levels benefits a mouse model of spinal muscular atrophy. *Neurobiol Dis.* 2008;31:361–7.
120. Burlacu A. Regulation of apoptosis by Bcl-2 family proteins. *J Cell Mol Med.* 2003;7:249–57.
121. Sareen D, Ebert AD, Heins BM, McGivern JV, Ornelas L, Svendsen CN. Inhibition of apoptosis blocks human motor neuron cell death in a stem cell model of spinal muscular atrophy. *PLoS One.* 2012;7:e39113.
122. Trülsch B, Garnett C, Davies K, Wood M. Knockdown of SMN by RNA interference induces apoptosis in differentiated P19 neural stem cells. *Brain Res.* 2007;1183:1–9.
123. Tsai MS, Chiu YT, Wang SH, Hsieh-Li HM, Lian WC, Li H. Abolishing Bax-dependent apoptosis shows beneficial effects on spinal muscular atrophy model mice. *Mol Ther.* 2006;13:1149–55.
124. Simic G, Seso-Simic D, Lucassen PJ, Islam A, Krsnik Z, Cviko A, et al. Ultrastructural analysis and TUNEL demonstrate motor neuron apoptosis in Werdnig-Hoffmann disease. *J Neuropathol Exp Neurol.* 2000;59:398–407.
125. Soler-Botija C, Ferrer I, Gich I, Baiget M, Tizzano EF. Neuronal death is enhanced and begins during fetal development in type I spinal muscular atrophy spinal cord. *Brain.* 2002;125:1624–34.
126. Lefrançois T, Fages C, Peschanski M, Tardy M. Neuritic outgrowth associated with astroglial phenotypic changes induced by antisense glial fibrillary acidic protein (GFAP) mRNA in injured neuron-astrocyte cocultures. *J Neurosci.* 1997;17:4121–8.
127. Pekny M, Lane EB. Intermediate filaments and stress. *Exp Cell Res.* 2007;313:2244–54.
128. Yang Z, Wang KK. Glial fibrillary acidic protein: from intermediate filament assembly and gliosis to neurobiomarker. *Trends Neurosci.* 2015;38:364–74.
129. Zhang S, Wu M, Peng C, Zhao G, Gu R. GFAP expression in injured astrocytes in rats. *Exp Ther Med.* 2017;14:1905–8.
130. Buffo A, Rite I, Tripathi P, Lepier A, Colak D, Horn A-P, et al. Origin and progeny of reactive gliosis: a source of multipotent cells in the injured brain. *Proc Natl Acad Sci.* 2008;105:3581–6.
131. DiSabato DJ, Quan N, Godbout JP. Neuroinflammation: the devil is in the details. *J Neurochem.* 2016;139(Suppl 2):136–53.
132. Jäkel S, Dimou L. Glial cells and their function in the adult brain: a journey through the history of their ablation. *Front Cell Neurosci.* 2017;11:24.
133. Moisse K, Strong MJ. Innate immunity in amyotrophic lateral sclerosis. *Biochim Biophys Acta.* 2006;1762:1083–93.
134. Rindt H, Feng Z, Mazzasette C, Glascock JJ, Valdivia D, Pyles N, et al. Astrocytes influence the severity of spinal muscular atrophy. *Hum Mol Genet.* 2015;24:4094–102.
135. McGivern JV, Patitucci TN, Nord JA, Barabas MA, Stucky CL, Ebert AD. Spinal muscular atrophy astrocytes exhibit abnormal calcium regulation and reduced growth factor production. *Glia.* 2013;61:1418–28.
136. Buffo A, Rossi F. Origin, lineage and function of cerebellar glia. *Prog Neurobiol.* 2013;109:42–63.
137. Cerrato V. Cerebellar astrocytes: much more than passive bystanders in ataxia pathophysiology. *J Clin Med.* 2020;9:757.
138. Wechsler-Reya RJ, Scott MP. Control of neuronal precursor proliferation in the cerebellum by Sonic Hedgehog. *Neuron.* 1999;22:103–14.
139. Xu H, Yang Y, Tang X, Zhao M, Liang F, Xu P, et al. Bergmann glia function in granule cell migration during cerebellum development. *Mol Neurobiol.* 2013;47:833–44.
140. White J, Sillitoe R. Postnatal development of cerebellar zones revealed by neurofilament heavy chain protein expression. *Front Neuroanat.* 2013;7:9.
141. Liedtke W, Edelmann W, Bieri PL, Chiu F-C, Cowan NJ, Kucherlapati R, et al. GFAP is necessary for the integrity of CNS white matter architecture and long-term maintenance of myelination. *Neuron.* 1996;17:607–15.
142. Ludwin SK. An autoradiographic study of cellular proliferation in remyelination of the central nervous system. *Am J Pathol.* 1979;95:683–96.
143. Baumel Y, Jacobson GA, Cohen D. Implications of functional anatomy on information processing in the deep cerebellar nuclei. *Front Cell Neurosci.* 2009;3:14.
144. Heck DH, De Zeeuw CI, Jaeger D, Khodakhah K, Person AL. The neuronal code(s) of the cerebellum. *J Neurosci.* 2013;33:17603–9.
145. Liu H, Lu J, Chen H, Du Z, Li XJ, Zhang SC. Spinal muscular atrophy patient-derived motor neurons exhibit hyperexcitability. *Sci Rep.* 2015;5:12189.
146. Simon CM, Janas AM, Lotti F, Tapia JC, Pellizzoni L, Mentis GZ. A stem cell model of the motor circuit uncouples motor neuron death from hyperexcitability induced by SMN deficiency. *Cell Rep.* 2016;16:1416–30.
147. Chiu K, Lau WM, Lau HT, So KF, Chang RC. Micro-dissection of rat brain for RNA or protein extraction from specific brain region. *J Vis Exp.* 2007;7:269.
148. Schneider CA, Rasband WS, Eliceiri KW. NIH image to ImageJ: 25 years of image analysis. *Nat Methods.* 2012;9:671–5.
149. Charvet CJ, Hof PR, Raghanti MA, Van Der Kouwe AJ, Sherwood CC, Takahashi E. Combining diffusion magnetic resonance tractography with stereology highlights increased cross-



- cortical integration in primates. *J Comp Neurol.* 2017;525:1075–93.
150. Chandar K, Freeman BK. Spinal cord anatomy. *Encyclopedia of the neurological sciences.* 2nd ed. Cambridge: Academic Press; 2014. p. 254–63.
 151. Hendy JP, Takahashi E, van der Kouwe AJ, Charvet CJ. Brain wiring and supragranular-enriched genes linked to protracted human frontal cortex development. *Cereb Cortex.* 2020;30:5654–66.
 152. Yendiki A, Aggarwal M, Axer M, Howard AFD, van Walsum AVC, Haber SN. Post mortem mapping of connectonal anatomy for the validation of diffusion MRI. *Neuroimage.* 2022; 256:119146.
 153. Fricker RA, Carpenter MK, Winkler C, Greco C, Gates MA, Björklund A. Site-specific migration and neuronal differentiation of human neural progenitor cells after transplantation in the adult rat brain. *J Neurosci.* 1999;19:5990–6005.

SUPPORTING INFORMATION

Additional supporting information can be found online in the Supporting Information section at the end of this article.

How to cite this article: Cottam NC, Bamfo T, Harrington MA, Charvet CJ, Hekmatyar K, Tulin N, et al. Cerebellar structural, astrocytic, and neuronal abnormalities in the SMN Δ 7 mouse model of spinal muscular atrophy. *Brain Pathology.* 2023;33(5):e13162. <https://doi.org/10.1111/bpa.13162>